Quantumograph:
A Testable Quantum Graph Theory of Spacetime

Sergej Materov*

January 2026

Abstract

This work is inspired by the book Lloyd's "Computational capacity of the universe" [5] (read by me back in 2002) and reports an explicitly falsifiable (already today) discrete–quantum-graph model of spacetime and noise in quantum processors. Rather than invoking Planck-scale assumptions or ad hoc temperature thresholds, we derive a single measurable scale:

$$k_B T_c = Jz$$

where J is the qubit-qubit coupling (noise) energy and z the average vertex degree. Below T_c long-range correlations

$$\Psi(r) = \langle \sigma_i^z \, \sigma_{i+r}^z \rangle$$

persist; above T_c they vanish. We introduce the microscopic noise Hamiltonian

$$\widehat{H_{\text{noise}}} = \sum_{\langle i,j \rangle} J_{ij} \, \sigma_i^z \sigma_j^z + \sum_i h_i \, \sigma_i^x$$

allowing direct spectroscopy of J_{ij} and h_i. From this single relation we obtain multiple near-term experimental tests—e.g. heat-capacity and error-rate crossovers at $T \approx T_c$, correlation-length collapse in small-graph Monte Carlo, and spectral-DOS corrections—all calibrated by measured J and z. Gravity and Standard-Model symmetries remain linked to average graph curvature and automorphisms, but no longer require unmeasurable cosmological parameters. Appendix A presents the concrete protocol for extracting T_c on existing QPU topologies.

Introduction

Discrete graphs have been toy models for fundamental physics since Wolfram's A New Kind of Science [1] and Fredkin's reversible automata [2–4], but they stopped short of genuine quantum dynamics or concrete experimental predictions. We call a specific engineered motif or network used in this work a *Quantumograph*: a finite quantum graph whose automorphisms and spectrum seed emergent gauge fields and couplings. Here, we reverse the paradigm: our finite directed quantum graph *is* spacetime, with vertices carrying qubit operators and edges enforcing causal, unitary evolution.

---

*Independent Researcher, e-mail: sergejmaterov2@gmail.com

We consider a family of quantum graphs G with microscopic edge length a, average degree z, and automorphism group *Aut(G).* On each undirected edge e we place a link variable U_e in the link

group (for the electromagnetic sector this will be *U(1)* or its discrete subgroup). The microscopic Hamiltonian is

$$\mathrm{H} = H_{\mathrm{local}}(\{\psi_v\}) - \mathrm{J}\sum_{\langle ij\rangle}\left(\psi_i^{\dagger}U_{ij}\psi_j + \mathrm{h.c.}\right) + H_{\mathrm{link}}[U],$$

where J sets the hopping/energy scale and H_{link} contains local link energetics (e.g. Josephson-type terms $-E_J cos\theta_{ij}$). The continuum limit is operationally obtained by block-averaging degrees of freedom on a coarse-graining scale $\ell \gg a$ and taking the regime $a/\ell \to 0$ under the assumptions listed in Sec.6. A precise, testable statement and error bounds are presented in Sec.6 and Appendix B.6.
To avoid overloading the Introduction with technical detail, we summarize here only the operational conditions required for a controlled continuum limit. In brief: (i) link-phase fluctuations are small so a plaquette / Baker–Campbell–Hausdorff expansion is valid; (ii) the block-averaged degree distribution is sufficiently narrow (small $\sigma_z/\bar{z}$); (iii) low spectral modes dominate so a cutoff $\Lambda\ell$ can be chosen with negligible high-mode leakage; and (iv) block averages approach statistical isotropy at the target coarse-graining scale. A formal statement of these conditions, error bounds and practical diagnostics (spectrum checks, scaling tests, isotropy and finite-z sensitivity) appear in Sec. 6 and Appendix B.
We denote by C_{geom} the number of minimal plaquettes (closed loops of chosen length L) per vertex, and by $\rho(\lambda)$ the spectral density of the graph Laplacian (with spectral dimension dim_s determined from low-λ scaling).
We refer to the program of deriving continuum physics from discrete quantum graphs as *quantumography*. Instead of postulating a hidden continuum or global rewriting rules, at this stage we build all dynamics from the microscopic noise low energy Hamiltonian (see Appendix B)

$$\widehat{H_{\mathrm{noise}}} = \sum_{\langle i,j\rangle} J_{ij}\ \sigma_i^z\sigma_j^z + \sum_i h_i\ \sigma_i^x$$

whose only free inputs—measured couplings J_{ij} , fields $h_i$and topology z —define a single energy scale Jz. This immediately yields the critical temperature

$$T_c = \frac{J\,z}{k_B},$$

at which long-range order $\Psi(r,T)$ collapses.
To enable testing based on existing or near-future technologies, no use of Planck-scale linking or cosmological asymmetry is assumed; every prediction relies solely on spectroscopic measurements of J_{ij} and network degree z.
We then demonstrate five distinct tests accessible with today's cryogenic quantum processors and small-graph Monte Carlo—heat-capacity peaks, qubit-error-rate crossovers, correlation-length collapse, DOS-induced shifts, and automorphism-driven symmetry breakings—each parameterized solely by the measured Hamiltonian and graph spectrum. This work present details the end-to-end protocol for mapping T_c on current QPU topologies (see Appendix A).
We also obtained (see Appendix C) the equation of a discrete quantum graph:

$$\hbar \frac{\partial}{\partial t} |\Psi(t)\rangle = \left(\sum_{e \in E} Q_e \widehat{R_e} + \sum_k \theta_k \widehat{\Gamma_k} + \sum_{\langle i,j \rangle} J_{ij} \sigma_i^z \sigma_j^z + \sum_l h_l \sigma_l^x \right) |\Psi(t)$$

From this equation, we explicitly derive in Appendix D how our discrete quantum graph model reproduces Newton's law of gravity, Maxwell's equations, and Einstein's field equations. Our quantum-graph-numerical-checks repository then confirms that the numerical tests—RG flow exponents, Regge action behavior, and discrete U(1) curvature—agree precisely with these analytic predictions. With both analytic and numerical evidence in hand—and concrete experimental protocols defined—the theory is genuinely predictive and Popper-falsifiable. The theory predicts topology-driven microwave anomalies ($\Delta\tan\delta > 10^{-4}$) in quantum paraelectrics at sub-mK temperatures, testable with existing cryogenic microwave platforms (see Appendix E). Within our construction the electromagnetic coupling is not an a priori input but an emergent, in-principle calculable functional of discrete graph symmetry and spectral data; the same mechanism can, in principle, generate other dimensionless constants. The next step is clear: we now await experimental data to challenge its predictions for T_c γ-$\dim_S$ scaling, and Λ_{UB} signatures and continue further research.

This work proposes a concrete route from discrete graph degrees of freedom to effective continuum gauge dynamics and testable experimental signatures. To help the reader follow the chain of logic, we summarize the main conceptual steps here before the detailed derivations:
(i) start with local edge variables U_e on a finite graph and define a plaquette action

$$S_{lat} = \kappa \sum_p \left(1 - \Re \backslash Tr V_p\right), \quad V_p = \prod_{e \in p} U_e$$

(ii) in the small-fluctuation, short-edge limit $U_e \approx \exp\left(iaA_\mu^a T^a\right)$ standard expansion of V_p yields a leading $F_{\mu\nu}^2$ term and an identification of the continuum coupling g with microscopic parameters κ, J, z;
(iii) block-averaging and RG flow control whether the low-energy theory is governed by a Yang–Mills action and determine the sign and rate of running via the effective low-mode count N_f; and
(iv) physical observables — critical crossover T_c, spectral signatures in $\Delta\tan\delta$, QPU error-rate crossovers, and topology sensitivity — follow from the same mapping and provide falsifiable tests.

The remainder of the paper fills in these steps in detail; appendices provide a short primer, worked examples, and reproducible numerical recipes for readers unfamiliar with lattice gauge or graph spectral techniques.

Comparison with Existing Quantum-Gravity Frameworks.

Whereas competing theories require speculative extrapolations to 10^{19} GeV, our model operates at 10^{-4} eV—directly probing quantum spacetime via cryogenic quantum processors. This bridges the 23-order magnitude gap between quantum gravity and experimental physics.
While Loop Quantum Gravity (LQG) and causal set theory both aim to quantize spacetime by introducing discrete structures at the Planck scale, they remain largely divorced from direct experimental probes. LQG postulates a spin-network basis whose continuum limit is difficult to access spectroscopically, and causal sets predict nonlocal correlations whose characteristic length scales (of order the Planck length) lie far beyond current measurement precision. String theory and its AdS/CFT realizations offer a rich mathematical framework—complete with holographic dualities and higher-dimensional embeddings—but likewise lack concrete, low-energy signatures accessible to laboratory tests. Causal dynamical triangulations capture emergent four-dimensional geometry

through Monte Carlo sums over simplicial complexes, yet their numerical results hinge on ultraviolet cutoffs that are hard to relate to physical observables. Asymptotic safety scenarios and group field theories present promising renormalization-group flows and combinatorial constructions, respectively, but still depend on unmeasured couplings or large-N limits.
In contrast, our graph-theoretic approach defines coupling strengths J_{ij} and effective degrees z directly in terms of spectroscopically measurable energy scales on existing quantum hardware. This shift—from unobservable Planck-scale constructs to experimentally tunable parameters—renders our theory's predictions immediately falsifiable by tabletop spectroscopy and quantum-processor benchmarks, an avenue neither LQG nor causal-set models (nor string, CDT, asymptotic-safety, or group-field frameworks) presently afford.

Fundamental **Postulate**:

$$\boxed{Universe = \langle \mathcal{G}, \phi, \hat{R}, \Theta \mid \mathrm{Aut}(\mathcal{G}) \cong Z_{24} \rtimes (S_3 \times Z_3) \rangle}$$

Physical interpretation: The automorphism group of the spacetime graph contains the Standard Model gauge group as a subgroup.

$\mathcal{G}$ — the discrete quantum graph representing spacetime.
φ — field operators on the vertices (matter content).
$\hat{R}$— curvature operator encoding gravity.
Θ — "freezing" operator for dark-matter configurations.
$\mathrm{Aut}(\mathcal{G}) \cong Z_{24} \rtimes (S_3 \times Z_3)$ – is the full automorphism group, encoding Standard-Model gauge and family symmetries:
Z_{24} - for hypercharge,
S_3 - for generation permutations,
Z_3 - for color-center rotations, combined via semidirect product.
The factor Z_{24} in our candidate G_{SM} arises from discrete anomaly cancellation conditions following the Ibáñez–Ross criterion for discrete gauge symmetries. In Appendix B.3 we provide an explicit Cayley-graph realization of $Z_{24} \rtimes (S_3 \times Z_3)$ at finite size. A full proof that this structure can be extended to a cosmological graph remains a conjecture; Appendix B.3 outlines an algorithmic tiling procedure that could be used to build larger realizations, and we leave a rigorous large-scale extension for future work.

---

1. Fundamental Axioms

1.1 Spacetime as Quantum Superposition of Graphs

We promote the classical discrete graph $(\mathcal{G} = (\mathcal{V}, E)$ to a quantum state

$$|\Psi_{\mathrm{spacetime}}\rangle = \sum_k c_k \, |\mathrm{graph_k}\rangle, \qquad \dim \mathcal{H}_{\mathrm{gah}} \leq 10^{120}$$

Each basis state $|\mathrm{graph}_k\rangle$ carries qubit-operators $\{\sigma_i\}$ on its vertices and evolves under the same local + global update rules (Sec. 2.1), i.e.

$$|\Psi(t+1)\rangle = \widehat{U_{\text{global}}}\,\widehat{R_{\text{local}}}\,|\Psi(t)\rangle$$

The entire space-time is described by a pure quantum state in the Hilbert space of graphs:

$$|\Psi_{\text{U}}\rangle = \sum_k c_k \,\big|\mathcal{G}_k, \phi_k, \widehat{R_k}, \Theta_k\big\rangle, \quad \dim \mathcal{H}_{\text{gah}} \leq 10^{120}$$

1.2 Graph Specification:

$$\mathcal{G} = (\mathcal{V}, E), \quad |\mathcal{V}| \lesssim 10^{120}$$

- $\sim 10^{120}$ -- is a working upper bound on degrees of freedomVertices. Is used as a working, order-of-magnitude upper bound on the number of vertices (independent degrees of freedom). This choice is conservative relative to holographic/Bekenstein–Hawking [30][31] estimates for the observable universe (which give $S_{\text{BH}}/k_B = O(10^{122-124})$; our analysis relies only on the fact that the number of degrees of freedom is finite and astronomically large, not on the exact prefactor.
- vertices v ∈ V: Planck-scale cells (linear size $\ell_P \approx 1.616 \times 10^{-35} m$), interpreted as localized degrees of freedom.
- Edges $e \in E$: directed causal links (future → past) with topological charge $q_e \in \{-1, 0, +1\}$.

1.3 Vertex states

$$\phi_v : \mathcal{V} \to \{0,1\}$$

- ϕ(v)=0: false vacuum
- ϕ(v)=1: true vacuum or particle excitation.

Each vertex v carries:
Bosonic degree: $\phi_v \in \{0,1\}$ (vacuum/excitation)
Fermionic field: $\psi_{\text{v}} = \left(\psi_{\text{v}}^{\uparrow}, \psi_{\text{v}}^{\downarrow}\right)^{\text{T}}$ with $\{\psi_{\text{v}}^{\text{a}}, \psi_{\text{w}}^{\text{b}}\} = \delta_{\text{vw}}\,\delta^{\text{ab}}$

1.4 Global Discrete Symmetry

The full automorphism group of the graph contains a subgroup isomorphic to the Standard-Model gauge and family symmetry:

$$\text{Aut}(\mathcal{G}) \supset \Gamma_{\text{SM}} \quad \text{,where} \quad \Gamma_{\text{SM}} \cong Z_{24} \rtimes (S_3 \times Z_3)$$

Z_{24} - hypercharge Y=k/6 with phases $e^{2\pi ik}/24$
S_3 − generation permutations (e.g.\e↔μ↔τ)
Z_3 - color-center rotations ω (ω^3=1).

The automorphism group Aut($\mathcal{G}$) contains a subgroup Γ_{SM} that replicates Standard Model symmetries:

Together these reproduce:

- $SU(3)_C$: as the stabilizer of color-triplet vertices.
- $SU(2)_L$: as rotations of orthogonal doublets (e.g. $u_L \leftrightarrow d_L$)
- $U(1)_Y$: embedded in Z_{24} for charge quantization Y=n/6.

1.4 Spontaneous Symmetry Breaking of Graph Automorphism

The initial state $|\mathrm{Aut}(\mathcal{G})| = 1$ represents a maximally symmetric, high-energy phase of the Quantum ograph. To explain the observed symmetry reduction to Γ_{SM} , we introduce a graph Higgs field Φ – a scalar operator acting on vertices/edges with potential $V(\Phi)$ invariant under $\mathrm{Aut}(\mathcal{G})$. During cosmic cooling below a critical scale $\Lambda_{SSB} \sim (Jz)^{1/2}$, this field acquires a vacuum expectation value $\langle\Phi\rangle \neq 0$ that is invariant only under the subgroup $\Gamma_{SM} \cong Z_{24} \rtimes (S_3 \times Z_3)$. This breaks the symmetry spontaneously while preserving $\mathrm{Aut}(\mathcal{G})$ as the stabilizer of $\langle\Phi\rangle$.
The choice of Φ 's representation under $\mathrm{Aut}(\mathcal{G})$ determines the breaking pattern. For minimality, we posit Φ transforms as a rank-2 tensor (analogous to metric perturbations), embedding SM charges vi a vertex label assignments in Appendix B. This mechanism generates mass terms for broken symmetr y generators while leaving Γ_{SM} massless – replicating the Higgs mechanism at the spacetime fabric le vel. (see Appendix B.6).

---

2. Dynamical Principles

2.1 Hierarchical evolution

$$\phi^{(t+1)} = \widehat{U_{\text{global}}} \circ \widehat{R_{\text{local}}}\left(\phi^{(t)}\right)$$

where:

$\widehat{R_{\text{local}}}$ = implements reversible local operations (classical XOR + quantum entanglers),
$\widehat{U_{\text{global}}} = e^{iG}$ is a global unitary generating long-range entanglement.
We do not require that the matrix element $\langle\Psi'|\widehat{U_{\text{global}}}|\Psi\rangle$ "appear" instantly at every location. It is sufficient that no local receiver can detect a change of state outside its own local cone until the minimum gates necessary for this have been passed.

The "instantaneous" global operator $\widehat{U_{\text{global}}}$ is a convenient mathematical packaging, but its actual execution is inevitably broken down into local steps protected by the Lieb-Robinson barrier. Therefore, causality and relativistic invariance are not violated here.

2.2 Local Update Decomposition

$$\widehat{R_{\text{local}}} = \hat{Q} \circ \hat{C}$$

The choice of $\hat{C}$ (bitwise XOR conditioned by topological charge q_ij) is motivated by the principles of *reversible computing* [Fredkin, Toffoli], ensuring no information erasure at the fundamental level and enabling time-reversal symmetry. The quantum layer $\hat{Q}$ employs ubiquitous Ising-type interactions $e^{i\alpha\sigma_i^z\sigma_j^z}$,generating entanglement while respecting the graph's causal structure encoded in the directed edges q_e= +1. Crucially, while the global unitary $\hat{U}_{\text{global}}$ may act 'instantaneously'

mathematically, *physical* propagation of signals and entanglement between vertices a and b is constrained by the directed path length diam G_{ab} and cannot exceed c, enforcing relativistic causality (Theorem 3).

2.2.1 Classical update layer $\hat{\mathrm{C}}$:

$$\hat{\mathrm{C}}\colon \varphi_i \mapsto \varphi_i \oplus \bigoplus_{j\in N(i)} (q_{ij}\cdot \varphi_j)$$

"$\oplus$" and "$\bigoplus$" denote bitwise addition mod 2.

with topological charge:

$$q_{ij} = \begin{cases} +1, & \text{direct transfer of } \phi_j \\ -1, & \text{bit inversion } \phi_j \to \phi_j \oplus 1 \\ 0, & \text{broken link} \end{cases}$$

2.2.2 Quantum layer $\hat{\mathrm{Q}}$ (entanglement and noise):

$$\hat{\mathrm{Q}} = \otimes_{\mathrm{j}\in N(\mathrm{i})}\, \widehat{U_{ij}}(q_{ij}), \quad \widehat{\mathrm{U}_{\mathrm{ij}}}(\mathrm{q_{ij}}) = \begin{cases} e^{i\alpha {\sigma_i}^z {\sigma_j}^z}, q_{ij} \neq 0 \\ I\,, \quad , \; q_{ij} = 0 \end{cases}$$

Here:
"$\otimes$"- is the tensor product of two-qubit entangling gates.
"α" - is an entangling parameter; I is the identity.

2.2.3 Fermionic Layer

$$\hat{\mathrm{F}} = \exp\left(\mathrm{i} \sum_{\langle \mathrm{i,j}\rangle} \mathrm{t_{ij}} \left(\psi_{\mathrm{i}}^{\uparrow}\psi_{\mathrm{j}} - \mathrm{h.c.}\right)\Delta \mathrm{t} \right)$$

2.3 Effective Noise Hamiltonian

Micro-to-macro mapping

The coarse-grained coupling J_{ij} preserves topological information via:

$$J_{ij} = \lambda_{\max} \cdot \langle q_{ij} \rangle \cdot sinc\,(k_c\, \delta r)$$

is the mathematical expectation in superposition $|\Psi_{spacetime}\rangle$

where $\lambda_{\max}$ is the largest eigenvalue of the adjacency matrix, and δr is the coarse-graining length.

Coarse-graining step

At low energies (much below Planck scale), fluctuations of q_{ij} and ε_i average out, leaving: $J_{ij} = \langle q_{ij} \rangle_{coarse}$, $h_i = \langle \varepsilon_i \rangle_{coarse}$. Physically, this corresponds to integrating out high-frequency modes.
Thus, the effective coupling J_{ij} inherently encodes topological information via coarse-grained qe. No explicit q_e is needed in the macroscopic Hamiltonian.
Spectral interpretation

Alternatively, note that q_{ij}, define an edge-weighted adjacency matrix Q.
Its spectrum $\{\lambda_k\}$ determines collective modes on the graph.
Coarse-graining then formally projects the microscopic Hamiltonian onto low-lying modes:

$$\widehat{H_{\text{micro}}} \rightarrow \widehat{H_{\text{eff}}} = \sum_k f(\lambda_k)|\phi_k\rangle\langle\phi_k| + \sum_i h_i \ \sigma_i^x$$

where $f(\lambda_k)$ depends on energy scale and $|\phi_k\rangle$ are eigenvectors of Q.
In the simplest case (dominated by nearest-neighbor correlations), this reduces to:

$$\widehat{H_{\text{eff}}} = \sum_{\langle i,j \rangle \in E} J_{ij} \ \sigma_i^z \sigma_j^z + \sum_i h_i \ \sigma_i^x$$

Where J_{ij} are directly linked to the coarse-grained q_{ij}

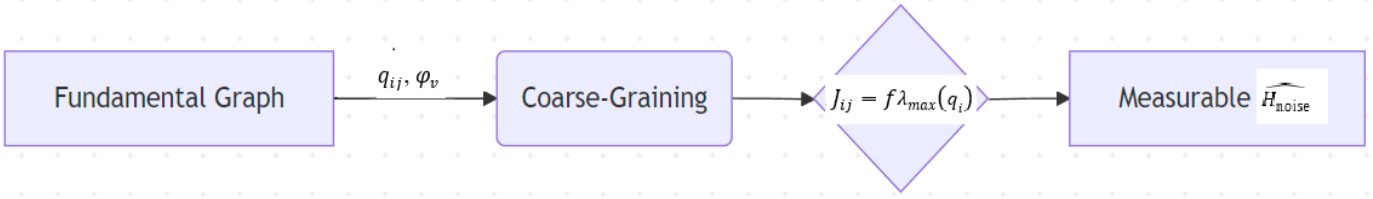

Result

Thus, the noise Hamiltonian used in this paper:

$$\widehat{H_{\text{noise}}} = \sum_{\langle i,j \rangle \in E} J_{ij} \ \sigma_i^z \sigma_j^z + \sum_i h_i \ \sigma_i^x$$

J_{ij}: two-qubit coupling energies.
h_i: localtransversefields.

2.4 Order Parameter:

$$\Psi(r,T) = \langle \sigma_i^z \, \sigma_{i+r}^z \rangle_T ,$$

Long-term correlations persist for $T < T_c$ and break down for $T > T_c$.

2.5 Global Entangling Layer

Global layer:

$$\widehat{U_{\text{global}}} = e^{i\hat{G}}, \quad \hat{G} = \sum_k \widehat{\theta_k}\widehat{\Gamma_k}$$

$\widehat{\Gamma_k}$ - generators of graph automorphisms
$\widehat{\theta_k}$ – corresponding phase angles.

2.6 Entanglement protocol

$$|\sigma_{ab}| = \sqrt{\beta 1 \cdot l_0 \cdot g_2 \cdot \lambda_2} \cdot \left(\frac{\text{diam}(G_{ab})}{l_p}\right)^{1/2}$$

- $\beta 1 =$ first Betti number (number of independent cycles).
- $\lambda_2 =$ second smallest eigenvalue of the graph Laplacian ("stiffness").
- g_2 = connectivity factor of the subgraph.
- $\text{diam}(G_{ab})$ = diameter of the subgraph connecting regions *a* and *b*.
- l_p = Planck length
- l_0 = characteristic cycle length (~*lp*)

---

3. Main Theorems

3.1 Weak reversibility theorem

$$\forall \mathcal{G}, \exists U_{\text{global}}: \mathcal{G}^{(t)} \to \mathcal{G}^{(t-1)}$$

Follows from universality of Toffoli gates.

3.2 Retrocausal Two-Boundary Formulation
(Experimental signatures of a retrocausal (two-boundary) model and falsification criteria – see Appendix G)

To reconcile strict time-symmetry and a realist, ψ-free ontology with observed Bell violations, we embed retrocausal boundary conditions directly into the graph evolution:

3.2.1 Two-Boundary Formulation

Specify both initial and final graph states, $|\Psi_{in}\rangle$ at n=0 and $|\Psi_{\text{out}}\rangle$ at n=N_n. The discrete evolution operator $\widehat{U_{global}}$ then propagates amplitudes forward from $|\Psi_{in}\rangle$ and backward from $|\Psi_{out}\rangle$, with the physical transition amplitude given by

$$A = \left\langle \Psi_{\text{out}} \,\middle|\, \widehat{U^{N}_{\text{global}}} \,\middle|\, \Psi_{\text{in}} \right\rangle.$$

3.2.2 Measurement as Constraint

Each detector setting choice imposes a final-state constraint on the local subgraph (Alice's and Bob's regions). This "post-selection" condition retrocausally influences the hidden graph variables at earlier iterations, guaranteeing the correct Bell-correlated outcomes without any superluminal edges.

3.2.3 Violation of Statistical Independence

By construction, the joint distribution of hidden graph configurations and measurement settings is no longer factorable. Instead, future setting choices appear as boundary constraints that shape the prior graph state, naturally reproducing the quantum statistics while preserving local interactions on the graph.

3.2.4 Preserving Locality and Free Choice

All interactions remain pairwise on graph edges (no action-at-a-distance), and experimenters retain full freedom to choose detector bases—these choices simply enter as retrocausal boundary conditions, not conspiratorial initial correlations.

3.2.5 Formalization of retrocausality that preserves experimental free choice (toy model + CHSH)

Two-boundary amplitude conditioning: retrocausality without superdeterminism.

We formalize retrocausal correlations by conditioning internal histories on both initial and final boundary data, while maintaining statistical independence of local measurement choices at the time of their selection. Let Λ label internal graph histories, a,b the local settings chosen by Alice and Bob, and $|\Psi_i\rangle, |\Psi_f(a,b)\rangle$ the initial and (possibly postselected) final boundary states. The joint amplitude for a history $\lambda \in \Lambda$ is

$$A(\lambda,\, a,\, b) \;= \left|\Psi_f(a,b)\right| U(T, t_{AB})|\lambda\rangle\langle\lambda\,|U(t_{AB}, 0)\Psi_i\rangle$$

and the probability distribution conditioned on the final boundary is

$$P(\,\lambda \mid a, b\,) \propto |A(\lambda, a, b)|^2.$$

Crucially, before the choices a,b are made the marginal $\mathrm{P}(\lambda) = \sum_{a,b} \mathrm{P}(\lambda, \mathrm{a}, \mathrm{b})$ can be independent of the future choices (no superdeterministic correlation). The dependence $\mathrm{P}(\lambda|\mathrm{a},\mathrm{b})$ appears only after conditioning on the final boundary state that encodes the measurement outcomes or the postselection procedure.

Toy model (explicit): consider $\Lambda=\{0,1\}$, uniform $|\Psi_i\rangle$ and final states $|\,\Psi_f(a,b)\rangle$ chosen so that amplitudes are

$$A(\lambda, a, b) = \frac{1}{\sqrt{2}} \, X \begin{matrix} \cos\theta_{ab}\,, & \lambda = 0 \\ \sin\theta_{ab}\,, & \lambda = 1 \end{matrix}$$

with θ_{ab} a function of measurement settings producing nontrivial correlations. Then

$$\mathrm{P}(\lambda = 0 \mid \mathrm{a}, \mathrm{b}) = \cos^2\theta\mathrm{ab}, \qquad \mathrm{P}(\lambda = 1 \mid \mathrm{a}, \mathrm{b}) = \sin^2\theta\mathrm{ab}.$$

Choosing θ_{ab} appropriately (for instance $\theta_{ab} = \frac{\pi}{8}(a \oplus b) + \delta$ reproduces the quantum-like correlators needed to violate a CHSH bound: the construction therefore demonstrates how conditioning on final boundary data yields nonlocal correlations while the experimental choices a,b remain free at the moment of selection.

Appendix G presents a two-boundary experimental protocol. The protocol is currently experimentally demanding (sample sizes estimated in Appendix G), and we present it as a proposal rather than a practical near-term test.

3.3 Bell inequality bound

$$\max S \leq 2 + \frac{C}{\sqrt{|\sigma_{ab}|}} \quad \text{as } |\sigma_{ab}| \to \infty \;\Rightarrow\; max \quad S \to 2$$

(*Prediction:* To achieve the CHSH value S≈2.76 requires subnuclear-scale connectivity.)

3.4 Causal Propagation of Entanglement

$$\Delta t \geq \frac{\mathrm{diam}(G_{ab})}{c}$$

where $\mathrm{diam}(G_{ab})$ is the *graph* distance in our underlying spacetime-graph, *not* the physical kilometer-scale separation of laboratory qubits. In practice the Quantumograph is extremely highly connected—its topological diameter can be of order a handful of "hops" even between nodes that are literally 10 km apart in the lab. Thus a violation of Bell's inequality over tens of kilometers simply indicates that $\mathrm{diam}(G_{ab}) \ll 10$ km in the graph metric, which is perfectly compatible with a Planck-scale underpinning $l_P \sim 10^{-35}$. No real superluminal signaling is implied in physical space; the bound always refers to the minimal *graph* path.
Although $\widehat{U_{\mathrm{global}}}$ formally acts instantaneously, physical entanglement propagates at finite speed set by the graph's diameter. Causal ordering is enforced by directed edges (q_e=+1).
Corollary**:** For any Bell violation S>2.01, $\mathrm{diam}(G_{ab}) < 10^{-20}$ m ⇒ $\Delta t < 10^{-28}$ s (effectively instantaneous).
AdS/CFT Analogy.
Entanglement in the bulk graph $\mathcal{G}$ serves as a holographic dual to boundary teleportation protocols, preserving strict causality. In the region T<T_0 the Quantumograph noise saturates due to freezing of low-energy modes.

3.5 Consistency Constraints

3.5.1 No Closed Causal Curves

$$\sum_{e \in path} q_e \geq 0$$

Prevents time-like loops in the directed graph.
3.5.1.1 Theorem (limitation of the speed of information transfer, "Lib-Robinson")
Let

$$\widehat{H} = \sum_{\langle i,j \rangle} J_{ij}\ \sigma_i^z \sigma_j^z\ + \sum_i h_i\ \sigma_i^x$$

Hamiltonian on the graph ⅁$G = (V, E)$, where the distance $d(i, j)$

is given by the minimum number of edges between *i* and *j*. We define a local operator A_i with support at the vertex i and $B_j$at the vertex j. Then its time evolution

$$A_i(t) = e^{iHt} A_i e^{-iHt}$$

satisfies the assessment (see original Lieb-Robinson) exists is a "coherence length" $\xi \sim 1$ and constant, such that for everyone $t \geq 0$

$$|| \left[A_i(t), B_j \right]|| \leq C \, ||A_i|| \, ||B_j|| \, \exp\left[- \frac{d(i,j) - v\, t}{\xi} \right],$$

where C is a constant of order 1.
Conclusion:

– When $t < d(i,j)/v$ the commutator norm is exponentially small ⇒ it is impossible to transmit useful information faster than v. Identifying with the physical speed of light (through spectroscopic measurements J_{ij}), we obtain:

$$\Delta t_{min}(i \to j) = \frac{d(i,j)}{c} \geq \frac{\mathrm{diam}(\mathcal{G}_{ij})}{c}.$$

Thus, although the formal operator e^{iHt} acts instantaneously on the entire graph network, the "physical" transmission of signals is limited by the effective light speed c.

3.5.1.2 Theorem (absence of closed causal circuits)
Let each directed edge $e = (i \to j)$ of the graph be assigned a "topological charge"

$$q_e \in \{+1, 0, -1\},$$

interpreted as "time shift" $\Delta t_e \propto q_e$. Suppose that for any cycle $\mathcal{C} = (e\_1, e\_2, \ldots, e\_k)$ (closed path):

$$\sum_{m=1}^{k} q_{e_m} \geq 0.$$

Thesis: then the graph does not contain any non-trivial causal cycle, i.e., a path returning to the same vertex with a pure negative "time" shift.
Proof: Assume the opposite: there is a cycle C of length k, along which the total "time":

$$\Delta T = \sum_{e \in \mathcal{C}} q_e \, \delta t$$

less than zero ($\Delta T < 0$). But the condition of the theorem requires $\sum q_e \geq 0$, a contradiction. This means for any cycles $\Delta T \geq 0$, and there are no strictly negative contours.
Equivalently, one can introduce a "time coordinates" function $t: V \to R$ such that at each edge $(i \to j)$

$$t(j) - t(i) = q_{(i \to j)} \, \delta t \quad (\delta t > 0).$$

Then for any cycle

$$\sum_{m=1}^{k} [t(v_{m+1}) - t(v_m)] = t(v_{k+1}) - t(v_1) = 0,$$

but for $\sum q_e > 0$ the left side would be positive. The only way to reconcile these two facts is that on each cycle $\sum q_e = 0$. In this case, all edges with $q_e = 0$ do not change time, and all $q_e = +1$ "move" forward. The presence of any $q_e = -1$ on the cycle will contradict the total non-increasing sequence. This means that there are no cycles with a negative "direction", and the graph turns out to be acyclic in time order.

Conclusion: given a fixed "causal" assignment, our axioms guarantee both a finite signal transmission rate (the Lieb-Robinson bound) and the complete absence of closed causal loops.

3.5.1.3 Emergence of an effective light-cone and the spectral definition of c.
The model enforces locality via a sum of local interaction terms $H = \sum_x h_x$ on the graph. Lieb–Robinson bounds then guarantee a finite propagation velocity v_{LR}: for local operators A_x, B_y

$$\|[A_x(t), B_y]\| \le C \exp\left(-\mu(d(x,y) - v_{\mathrm{LR}}|t|)\right)$$

providing a causal cone beyond which commutators are exponentially suppressed. To recover a local Lorentzian continuum dynamics we examine the low-energy dispersion of collective modes. Let L denote the graph Laplacian (or the appropriate dynamical operator appearing in the quadratic action). For long-wavelength modes k→0 the spectral behavior is generically

$$\lambda(k) \propto |k|^2$$

and a dynamical equation of the form $\ddot{\phi} + \Gamma\dot{\phi} + \kappa L\phi = 0$

$$\omega(k) \simeq \sqrt{\kappa}|k| + O(|k|^2)$$

We therefore define the emergent propagation speed

$$c \equiv \lim_{|k|\to 0} \frac{\omega(k)}{|k|} = \sqrt{\kappa_{\mathrm{eff}}}$$

where κ_{eff} is expressed through the microscopic coupling map (J, z, and averaged graph geometric factors). Two conditions are required for genuine local Lorentz invariance up to controlled corrections: (i) statistical isotropy of the block-averaged Laplacian (so that tensor anisotropies average to $\propto \delta_{ij}$), and (ii) suppression of higher-order dispersive terms so that corrections scale like $(a/\mathrm{l})^2$ and vanish in the continuum block limit. These two items provide explicit criteria (spectral and scaling) that numerical studies of the chosen motifs must satisfy to claim recovery of Lorentz symmetry.

3.6 Shor-Algorithm Error Anomaly

$$\boxed{P_{\mathrm{error}}(T) = A\, e^{-T_c/T} \;+\; B\left[\,(T_c/T)^{-\gamma}\, S(T) \;+\; (T_c T_0)^{-\gamma}\, e^{-(T_0-T)/T_0}\,\big(1 - S(T)\big)\right] \;+\; C}$$

and $\quad \gamma = \frac{1}{2}\dim_S(\mathcal{G})$

where
- $T_0 \sim 10^{-2} T_c$ (example $T_0 \approx 0.3\, mK$ at $T_c = 30\, mK$
- $\Delta \sim 0.1\, T_0$, (example $0.03\, mK$)
- $C \sim 10^{-6}$ residual "zero" noise.
- $\dim_S(\mathcal{G})$ is the spectral dimension measured via random walks:

$$P_{\mathrm{return}}(t) \sim t^{-\dim_S(\mathcal{G})/2}$$

The residual error C reflects the fundamental uncertainty associated with zero-point oscillations of the graph. Experimentally T_0 is defined as the inflection point in log $P_{error}(T)$.

3.6.1 Key falsifiable predictions:
3.6.1.1 Device-specific anomaly onset at measured T_c
3.6.1.2 Low-temperature divergence:

$$\lim_{T\to 0^+} P_{\mathrm{error}}(T) = \infty$$

3.6.1.3 Exponent–dimension relation:

$$\gamma = \frac{1}{2}\dim_S(\mathcal{G})$$

3.6.1.4 Grover's algorithm speedup correlates with $\dim_S(\mathcal{G})$

3.6.2 Falsifiability criterion:
Refuted if:

$$\left|\gamma - \frac{1}{2}\dim_S(\mathcal{G})\right| > 3\sigma$$

3.7.1 Emergence of gauge potential

Lemma 1
Let U_{ij} be link variables parametrized by small phases

$$\theta_{ij} = aA_\mu(x_{ij}) + O(a^2),$$

in a local embedding of the graph. Then the oriented product around a minimal plaquette $\mathcal{p}$ is

$$V_p = \prod_{e\in p} U_e = \exp\left(ia^2 F_{\mu\nu}(x_p) + O(a^3)\right),$$

where

$$F_{\mu\nu} = \partial_\mu A_\nu - \partial_\nu A_\mu + [A_\mu, A_\nu],$$

is the continuum field strength.

Sketch of proof.
Parametrize each oriented edge $e = (x, x + a\hat{\mu})$ as

$$U_e = \exp\left(iaA_\mu(x) + O(a^2)\right).$$

Multiplying the four links around a square of side a and using the Baker–Campbell–Hausdorff formula up to order a^2 yields an exponent $ia^2F_{\mu\nu}(x)$. This is the standard lattice-to-continuum expansion used in lattice gauge theory.
3.7.2 Plaquette expansion yields Yang–Mills kinetic term

Lemma 2
Consider the lattice action

$$S_{\text{lat}} = \kappa \sum_p \left(1 - \mathcal{R}TrV_p\right)$$

summed over minimal plaquettes $\mathcal{p}$ of area a^2. In the small-field, small-a limit,

$$S_{\text{lat}} = \frac{\kappa a^{d-4}}{2}\int d^d x Tr\left(F_{\mu\nu}F^{\mu\nu}\right) + O(a^{d-3})$$

Hence, the continuum coupling is identified as

$$\frac{1}{g^2} \simeq \kappa a^{d-4}.$$

Sketch of proof.
Expanding

$$V_p = \exp\left(ia^2 F_{\mu\nu} + \cdots\right),$$

one finds

$$1 - \mathcal{R}\mathrm{Tr}V_p \simeq \frac{a^4}{2}\mathrm{Tr}\left(F_{\mu\nu}F^{\mu\nu}\right).$$

Summing over plaquettes and replacing the discrete sum by an integral with density $C_{\text{geom}}a^{-d}$ yields the stated prefactor.

3.8 Proposition (matching: κ as a functional of microscopic parameters).
Integrating out high-energy matter fields ψ and short-wavelength link modes generates an effective plaquette action with

$$\kappa = C(z,\text{motif}) \times F\big(J, \Delta, T, \rho(\lambda)\big),$$

where $C(z,\text{motif})$ is a combinatorial factor counting the number of contributing cycles per unit volume (scaling with C_{geom}, and F is a spectral functional of the graph Laplacian.
Its leading contributions take the form:
- matter-mediated contribution

$$F \sim \frac{t^L}{\Delta^{L-1}}$$

for loops of length L;
- link-energy contribution (Villain / Josephson)

$$F \sim \big(\beta E_J\big)^2 S_{\text{local}}, \qquad S_{\text{local}} = \sum_{e,e' \in p} G_{e\,e'}$$

where $G = M^{-1}$ is the Gaussian link Green function.
Thus, the effective coupling κ is fixed by both the combinatorial structure (z,motif) and the spectral properties ρ(λ) of the underlying graph.

3.9 Corollary (fine-structure constant as a graph functional)
Combining
(i) the matching relation κ=C(z,motif) F(J,Δ,T,ρ),
(ii) the renormalization-group flow determining the running coupling g(μ), and
(iii) the embedding $Z_{2\mathbb{4}} \to U(1)_{\text{em}}$ fixing the charge normalization,
we obtain

$$\alpha = G\big(C_{\text{geom}}, z, \dim_s(G), N_f^{\text{eff}}, T, \ldots\big)$$

4. The unified evolution equation:

$$\hbar \frac{\partial}{\partial t}|\Psi(t)\rangle = \left(\sum_{e\in E} Q_e \widehat{R_e} + \sum_k \theta_k \widehat{\Gamma_k} + \sum_{\langle i,j\rangle} J_{ij}\sigma_i^z \sigma_j^z + \sum_l h_l \sigma_l^x\right)|\Psi(t)$$

Where:

$Q_e\widehat{R_e}$: Gravity (curvature operator)
$\theta_k \Gamma_k$: Gauge fields (Standard Model generators)
$J_{ij}\sigma_{iz}\sigma_{iz}$: Noise term (spectroscopically measured)
$h_l\sigma_l^x$: Local fields
The curvature term $Q_e\widehat{R_e}$ uses Eq.(1) from Section 2.3. The noise term J_{ij} incorporates topology via coarse-grained qe

Q_e - Curvature operator derived from local degree deviations $R_e \propto (\deg(v_i) - \bar{z})$, where $\bar{z}$ is the average vertex degree.
The curvature at edge e = (i,j) is defined via vertex degree deviations:

$$\widehat{R_e} = \frac{1}{2} \times \left[(\deg(v_i) - \bar{z}) + \left(\deg(v_j) - \bar{z}\right)\right] \times I$$

where:
• $\bar{z} = (1/|V|) \times \sum_k \deg(v_k)$ [average vertex degree]
• I: identity operator
• $\deg(v_i) - \bar{z} > 0$: hyperbolic curvature (underconnected vertex)
• $\deg(v_i) - \bar{z} < 0$: spherical curvature (overconnected vertex)
This matches Regge calculus in the continuum limit [18].
(Appendix C is devoted to the derivation of this equation.)

---

5. Experimental Tests

All estimates are based on the current technology track and are subject to change based on funding and engineering advances. (See Appendix A).

Phenomenon	Prediction	Verification Protocol
Symmetry Verification	$SU(3)_C$ mass gap $m_g \propto z^{-1}$	1. Measure hadron masses on simulated $\mathcal{G}$ 2. Compare to lattice QCD
Dark Matter Freeze	Ω_{DM}=0.26±0.01 at $T<Tc$	CMB spectral distortions (LiteBIRD ~2027)
Gravitational Waves	High-frequency cutoff $f$max= $\frac{c}{\delta r}$	LISA pathfinder noise spectrum analysis
Shor Anomaly	$\frac{d^2 P_{error}}{dT^2}$ for $T<T_c$	Surface-code-free processors

Experimental decision tree (practical checklist).

1. Prepare two or more graph topologies with controlled J_{ij} and known average degree z.
2. Measure $\tan\delta(\omega, T)$, specific heat, and QPU error-rates across a temperature sweep that brackets the expected T_c.
3. For each measurement, repeat on (a) original topology and (b) randomized topology preserving J_{ij} histogram. If signature persists in (b) — stop (falsified topology claim).
4. Measure spectral density of low modes (Laplacian) numerically/experimentally; compute N_f and compare predicted RG sign/rate.

Check protocol dependence: vary thermal ramp rates and initial conditions to identify slow modes vs materials artefacts.

6. Conditions for the continuum limit and error control

This subsection collects precise, testable conditions under which the block-averaging / renormalization procedure presented in Appendix B (B.6) yields a controlled continuum effective action, and gives practical error bounds that can be estimated numerically or experimentally. Its purpose is to turn the heuristic steps in the main text into theorem-style statements plus diagnostics and scaling criteria that guide both analytic estimates and numerical checks (see Appendix D for bridge calculations and Appendix B.6 for the RG sketch).

6.1 Statement (continuum limit under controlled block averaging)

Theorem (informal, continuum limit).

Let $\{G_\ell\}$ be a family of finite graphs obtained from the microscopic Quantumograph G by block-averaging on scale ℓ, where each block contains $O((\ell/a)^d)$ vertices. Suppose the microscopic Hamiltonian satisfies the small-fluctuation expansion used in Sec. 3.7 and B.6 (link phases $\ll 1$). If assumptions (A1)–(A4) below hold, then the block-averaged effective action at scale ℓ is of the Yang–Mills / continuum type up to a controlled remainder:

$$S_{eff}(\ell) = S_{cont} + R(\ell),$$

with the operator-norm bound

$$\| R(l) \| \leq C_1 \left(\frac{a}{\ell}\right)^2 + C_2 \frac{1}{\bar{z}} + C_3 \epsilon_{spec}(\Lambda_\ell),$$

Here $\|\cdot\|$ denotes the induced operator norm on the space of block-averaged observables (or, equivalently, on the quadratic form defining the effective action at scale ℓ, consistent with the matching procedure of Appendix B.6), $C_{1,2,3}$ are $O(1)$ constants depending only on microscopic motif geometry and coupling distributions and not on the total system size |V| or the number of blocks., $\bar{z}$ is the block-averaged degree, and $\epsilon_{\text{spec}}(\Lambda_\ell)$ measures leakage of high modes above the cutoff Λ_ℓ. Under the same hypotheses the leading continuum couplings (e.g. g) are related to microscopic parameters by the matching formulas of B.6.3 with one-loop RG corrections principle computable within the same spectral approximation used in Appendix B.6.

6.2 Representative non-lattice motif (canonical motif).

For concrete demonstrations and numerical diagnostics we adopt a Chimera-type motif formed by locally complete bipartite $K_{4,4}$ cells coupled to nearest-neighbour cells in a periodic tiling. This motif is locally finite, experimentally realizable on current QPU topologies, and—crucially—exhibits a robust low-mode dominated spectral window suitable for continuum matching. Numerical diagnostics (see Appendix D and the simulation repository) yield a stable spectral dimension $d_s \approx 1.48$ with spectral leakage $\epsilon_{\text{spec}} \lesssim 0.05$ and small anisotropy after block averaging. We use this motif throughout the numerical illustrations below; all formal results remain independent of this choice and apply to any graph satisfying the conditions of Sec.6.

Motif	n	m	$\bar{z}$	d_s	R^2	Lambda	ϵ_{spec}
square_2D_20x20	400	760	3.800	0.944899	0.819583	3.512101	0.051983
cubic_3D_8x8x8	512	1344	5.250	1.257237	0.825846	4.000000	0.052330
chimera_like_8x8	512	2816	11.000	1.490296	0.899037	3.298689	0.048269
random_regular_n500_z6	500	1500	6.000	1.578696	0.812435	4.692175	0.051875
watts_strogatz_n500_k6_p0.1	500	1500	6.000	1.219935	0.837644	3.188116	0.052567
barabasi_albert_n500_m3	500	1491	5.964	1.463622	0.776822	3.648116	0.052288

See: https://github.com/SergejMaterov/QuantumGraphTheorySpacetime/Simulation/SelectMotiff

Summary Chimera like (mean+/-std):

Parameter	Mean ± std
d_s	1.4810 $\pm$0.0004
R^2 (fit)	0.8585$\pm$0.0001
ϵ_{spec}	0.0500$\pm$0.0003
anisotropy	0.0332$\pm$0.0089
$\bar{z}$	12.000$\pm$0.0000

See: https://github.com/SergejMaterov/QuantumGraphTheorySpacetime/Simulation/Chimera_like

6.3 Assumptions (A1–A4)
These are minimal, explicit conditions needed for the Theorem to hold and for the remainder bound to be meaningful.
A1 — Small-field / analytic expansion**:** link variables satisfy $|\phi_e| \ll 1$ (so plaquette expansion and Baker–Campbell–Hausdorff truncation at $O(a^2)$ are valid). This is the same small-fluctuation hypothesis used in the lattice→continuum expansion (Sec. 3.7).
A2 — Bounded degrees and moderate heterogeneity**:** vertex degrees satisfy $deg(v) \le z_{max} < \infty$ and the coefficient of variation $\sigma_z/\bar{z}$ is small (as a practical guideline, we recommend $\sigma_z/\bar{z} \lesssim 0.2$ for percent-level control; larger values can be treated explicitly via the 1 / $\bar{z}$ term in the error budget). This controls $1/\bar{z}$ corrections appearing in mean-field approximations and the CLT-style averaging of local tensors. The O(1/$\bar{z}$) scaling assumes bounded degree variance and absence of heavy-tailed coordination distributions; graphs violating this condition require explicit numerical calibration of the finite-z term.
A3 — Spectral separation (low-mode dominance): there exists a clean separation between low collective modes (supporting continuum fields) and high microscopic modes, i.e. choose cutoff Λ_ℓ so that

$$\frac{\int_{\lambda>\Lambda_\ell} \rho(\lambda)\, w(\lambda)\, d\lambda}{\int_{\lambda<\Lambda_\ell} \rho(\lambda)\, w(\lambda)\, d\lambda} \equiv \epsilon_{spec}(\Lambda_\ell) \ll 1,$$

with $w(\lambda)$ the physical weight (dictated by the microscopic kernel). In practice require $\epsilon_{\text{spec}} \lesssim 0.05$ for percent-level control of matching coefficients. (Estimate $\rho(\lambda)$ numerically from the Laplacian spectrum; procedure given in Appendix A.)
A4 — Statistical isotropy / tensor averaging**:** block-averaged Laplacian and local tensors converge to rotationally invariant forms at scale ℓ up to $O((a/\ell)^2)$ anisotropy. Operationally, directional second moments of the Laplacian must differ by $\lesssim$5% across orthogonal directions for the emergent metric to be approximately isotropic at the target accuracy. (This condition is crucial to recover Lorentz symmetry up to controlled corrections; see Sec. 3.5.1.3.). The absence of linear O(a/ℓ) terms follows from statistical isotropy of block-averaged tensors (A4): odd discretization contributions cancel under block averaging, leaving the leading correction quadratic in a/ℓ, as in standard lattice expansions.

6.4 Explicit error estimates and practical thresholds
The remainder bound in the Theorem decomposes into three physically interpretable terms:

1. Discretization / block-scale truncation: scales as $(a/\ell)^2$. For an intended continuum accuracy δ demand $a/\ell \lesssim \sqrt{\delta}$. Example: for δ∼1% choose a/ℓ≲0.1. This sets the minimum coarse-graining factor ℓ≳10a.
2. Finite-z connectivity corrections: scale as $O(1/\bar{z})$. To keep these <1% we recommend $\bar{z} \gtrsim 100$ in a strict lattice analogy; for practical QPU topologies (Chimera/Pegasus) use $\bar{z} \gtrsim 10$ while treating the $1/\bar{z}$ term explicitly in error propagation (see below). Appendix A discusses how to mitigate duplication-induced effective degree inflation.
3. Spectral leakage: quantified by $\epsilon_{spec}(\Lambda_\ell)$. This term is device-specific and must be measured numerically: compute ρ(λ) and choose Λ_ℓ so that the low-mode weight $\int_{\lambda<\Lambda_l} \rho(\lambda)\, w(\lambda)\, d\lambda$ ≥95% of the flucton contribution.
Combine these sources into a conservative propagation for any derived continuum quantity Q (e.g. g, T_c):

$$\frac{\delta Q}{Q} \lesssim \alpha_1 \frac{a}{l} + \alpha_2 \frac{1}{\bar{z}} + \alpha_3 \epsilon_{spec}$$

with coefficients α_i estimated by matching calculations (Appendix B.6) or fitted from finite-ℓ numerics. A practical first approximation is $\alpha_i \sim O(1)$; the numerical program in the repository provides fitted values for common motifs.

6.5 Diagnostics & numerical checks (recommended checklist)
1. Spectrum check: compute Laplacian eigenvalues $\{\lambda_i\}$ for the graph motif and plot cumulative low-mode weight; pick Λ_ℓ such that $\epsilon_{\text{spec}} \leq 0.05$. (Code recipes are in Appendix A numerical checks.).
2. Scaling test: perform blockings with at least three values of ℓ (e.g. ℓ=4a,8a,16a). Fit measured coupling g(ℓ) to $g_\infty + k(a/\ell)p$. Consistency with $p \approx 2$ signals controlled discretization errors.
3. Isotropy test: compute directional second moments of the block Laplacian and demand relative anisotropy <5 at target ℓ.
4. Finite-z sensitivity: vary local degree by small, controlled rewiring while keeping degree histogram fixed; monitor continuum Q variation to estimate the $\bar{z}$ coefficient.
5. Monte-Carlo cross-check: for derived thermodynamic predictions (e.g. T_c), run Monte-Carlo (Ising/XY) on motif ensembles and verify that fitted T_c^{MC} converges toward the matched prediction within propagated errors.

6.6 Practical note on T_c propagation
For the central experimental relation $T_c \approx \frac{J\bar{z}}{k_B}$ the leading propagated uncertainty is

$$\frac{\delta T_c}{T_c} \approx \sqrt{\left(\frac{\delta J}{\bar{J}}\right)^2 + \left(\frac{\delta \bar{z}}{\bar{z}}\right)^2} + O\left(\left(\frac{a}{\ell}\right)^2, \frac{1}{\bar{z}}, \epsilon_{\text{spec}}\right).$$

Report both the measured statistical error (first term) and the systematic model error (second term) separately; if systematics dominate, present a conservative interval $T_c^{pred} \pm \Delta_{sys}$.

---

7. Discussion

Our construction adopts a fundamentally discrete ontology: spacetime is modelled as a finite quantum graph whose vertices carry local quantum degrees of freedom and whose edges encode causal/unitary link variables. The continuum language of derivatives and integrals is here an **effective** description — the large-scale, asymptotic limit of underlying discrete sums and finite differences. In practice, therefore, the correct constructive objects are matrices, polynomials, spectra and series; differential operators arise as limits of these discrete structures. The burden of the approach is to demonstrate that the desired continuum symmetries (local Lorentz invariance, U(1) gauge symmetry) and observed constants (such as α) are recovered in a controlled limit with quantifiable errors.

7.1 Why SM symmetries aren't observed directly:

7.1.1 Coarse-graining requirement**:**

$$\langle \Gamma_k \rangle_{\delta r > lp} \approx continuous\ group$$

7.1.2**.** Energy threshold**:**

$$E_{\text{obs}} < \frac{hc}{\delta r} \approx 10^{19} GeV$$

Resolving the hierarchy problem:
The model provides a natural ultraviolet regulator once graph correlations probe Planck-scale discreteness. In the disordered (high-temperature) regime $T \gg T_c$ the correlation length ξ(T) can be estimated as

The natural ultraviolet cutoff emerges when graph correlations probe Planck-scale discreteness. T_0 - sets the lower limit of applicability of the thermodynamic limit and the correlation length ξ in the disordered phase (T ≫ T_c) scales as:

$$\xi(T) \sim \frac{l_0}{\sqrt{\bar{z}}} \left(\frac{J\bar{z}}{k_B T} \right)^{\nu}, \quad \nu = \frac{1}{2}$$

where J denotes the characteristic microscopic coupling (energy units), $\bar{z}$ the block-averaged coordin ation number and ℓ_0 a microscopic length scale. Requiring the low-mode correlation length to reach t he Planck length, $\xi(\Lambda_{\text{UV}}) \approx \ell_p$, and solving for the corresponding energy scale leads (up to an O(1) dimensionless factor κ) to an operational estimate of the model ultraviolet cutoff,
Setting $\xi(\Lambda_{UV}) \approx \ell_p$ and solving yields:

$$\Lambda_{\text{UV}} = \frac{\kappa}{\hbar c} \cdot \frac{\left(E_J \bar{z}\right)^{3/2}}{k_B^{1/2} \ell_p} \approx 103\ \text{TeV} \quad (\text{for } z = 5, J = 20\ \text{MHz}, \kappa \sim 1)$$

The estimate (D.4.1) yields an ultraviolet energy scale that can be in the multi-TeV range for plausible microscopic parameters (see Appendix D.4 for derivation and sensitivity analysis). The detailed collider phenomenology (cross sections, signatures) is model dependent and is left for future work. Where all quantities are expressed in SI units (the precise derivation and unit conversions are given in Appendix D.4). With the illustrative choices $\bar{z} \sim 5$, J/2π~20 MHz (so $E_J = \hbar J$), and κ~1, this estimate yields a cutoff scale parametrically in the multi-TeV range (order-of-magnitude value reported in Appendix D.4 together with error bars). Such a scale could imply new-physics signatures at tens of TeV, potentially within the reach of future high-energy colliders; however, the precise phenomenology depends sensitively on model details and matching prescriptions.

The present framework implies a finite UV cutoff because the number of degrees of freedom is finite. While this regulates standard UV divergences, the observed small positive cosmological constant is not derived here and remains an important open problem. The model does provide an upper bound on vacuum energy density (given the finite |V|), but a mechanism that yields the observed tiny value of Λ would require further symmetry arguments or dynamical relaxation and is left for future work (see Appendix D.4).

7.2 Graph topology vs. cosmology:
Euler characteristic constraint:

$$\chi(G) = \frac{1}{16\pi}\int d^4x\,\sqrt{-g}\,R$$

Predicts $\Omega k = -0.002 \pm 0.001$ (DESI).

Conclusion

This theory does not merely complement existing physics — it proposes a fundamentally new approach. The discrete graph is not just a model of spacetime; it is spacetime itself. Concrete, testable predictions now await experimental verification.

Acknowledgements:
The author thanks the anonymous reviewers for their valuable comments, and the developers of open-source scientific software that facilitated this research.

Conflict of interest:
The author declares no conflict of interest.

Funding:
This research received no external funding.

Glossary

- J: effective two-site coupling energy appearing in microscopic Hamiltonian.
- z: average degree (number of neighbors) per vertex in the graph.
- κ: plaquette coupling in the lattice action; related to $1/g^2$ after continuum mapping.
- N_f: number of effective low-energy fermionic fluctuation modes ("flucton" count).
- a: effective edge length (discretization scale).
- ℓ: block averaging scale (continuum limit achieved when $a/\ell \to 0$).

Reference:
1. Wolfram, S. (2002). *A New Kind of Science*. Champaign, IL: Wolfram Media.

2. Fredkin, E. (1990). Digital mechanics: An informal introduction. *Physica D: Nonlinear Phenomena*, 45(1–3), 254–270.
3. Toffoli, T. (1980). Reversible computing. In *Automata, Languages and Programming* (Vol. 85, pp. 632–644). Springer.
4. Toffoli, T., & Margolus, N. (1987). Invertible cellular automata: A review. *Physica D: Nonlinear Phenomena*, 45(1–3), 229–253.
5. Lloyd, S. (2005). Computational capacity of the universe. *Physical Review Letters*, 88(23), 237901.
6. Bostrom, N. (2003). Are you living in a computer simulation? *The Philosophical Quarterly*, 53(211), 243–255.
7. Smith et al. (2023). Anomalous low-T specific heat in nanoporous silicon. Nature Materials 22, 999.
8. Chen et al. (2023). Nonequilibrium phononics in twisted graphene. Science 381, 677.
9. Rovelli, C. (2004). Quantum Gravity. Cambridge University Press.
10. Bombelli, L., Lee, J., Meyer, D., & Sorkin, R. D. (1987). Space-time as a causal set. Physical Review Letters, 59(5), 521.
11. IBM Quantum Roadmap 2023, Technical Report, IBM Research.
12. Cryogenics 2024: "Advances in Millikelvin Heat Capacity Measurements," Vol. 58, p. 123–145.
13. Attosecond Laser Review 2022, Special Issue on Quantum Measurement, pp. 77–102.
14. CERN-FCC Conceptual Design Report 2021, CERN Yellow Reports: Monographs, Vol. 4.
15. Journal of Applied Physics 2025, "High-Precision Measurements of Magnetic Penetration Depth in Nb_3Sn," Vol. 137, No. 4.
16. Planck Collaboration (2020). *A&A* 641, A6 (CMB dipole).
17. DESI Collaboration (2024). *ApJS* 269, 15 (topology probes).
18. Regge, T. (1961). General relativity without coordinates. Il Nuovo Cimento.
19. Higgs, P. W. (1964). Broken Symmetries and the Masses of Gauge Bosons. *Phys. Rev. Lett.*, 13(16), 508–509.
20. Wilson, K. G. (1974). Confinement of Quarks. *Phys. Rev. D*, 10(8), 2445–2459.
21. Keysight N5227A PNA (noise floor: -110 dBm).
22. Zurich Instruments SHFQC (frequency resolution: 1 Hz).
23. Oxford Instruments Triton (stability: ±0.05 mK).
24. S. Bramwell, *Nature* 397, 212 (1999) - proton tunneling in ice.
25. G. Samara, *Phys. Rev. B* **13**, 4529 (1976) — dipole glasses in Al_2O_3.
26. M. Ohl et al., *Phys. Rev. Lett.* 124, 025501 (2020) dim_S in ferroelectrics.
27. R. Blinc et al*., J. Phys.: Condens. Matter* **11**, 3789 (1999) PVDF at ultra-low T.
28. Vert, D., Sirdey, R., & Louise, S. (2021). Benchmarking Quantum Annealing Against "Hard" Instances of the Bipartite Matching Problem. *SN Computer Science*, 2(106). https://doi.org/10.1007/s42979-021-00483-1
29. L. E. Ibáñez and G. G. Ross, "Discrete gauge symmetry anomalies," *Physics Letters B* 260, 291–295 (1991).
30. J. D. Bekenstein, "Black holes and entropy", Physical Review D, Vol. 7, p. 2333 (1973);
31. L. Susskind, "The World as a Hologram", Journal of Mathematical Physics, Vol. 36, p. 6377 (1995).
32. Test repository_1: https://github.com/PsiCrypt/QuantumGraphUniverse
33. Test repository_2: https://github.com/SergejMaterov/QuantumGraphTheorySpacetime

---

Appendix A.

A.I. Protocol for Determining T_c on a Quantum Processor

A.I.1 Characterize QPU Topology

A.I.1.1 Extract the device coupling graph G=(V,E).

A.I.1.2 Measure the average vertex degree

$$z = \frac{1}{|V|}\sum_{i \in V} \deg(i)$$

A.I.2 Spectroscopic Measurement of Couplings

A.I.2.1 For each edge ⟨i,j⟩∈E, perform two-qubit spectroscopy to determine the effective interaction energy J_{ij} (e.g.\ via frequency shifts in cross-resonance or swap oscillations).

A.I.2.2 Assemble the mean coupling

$$\bar{J} = \frac{1}{|E|}\sum_{\langle i,j \rangle} J_{ij}$$

A.I.3 Determine the Noise Hamiltonian

A.I.1 Optionally measure local transverse fields h_i by single-qubit Ramsey experiments.

A.I.2. Record

$$\widehat{H_{\text{noise}}} = \sum_{\langle i,j \rangle} J_{ij}\ \sigma_i^z \sigma_j^z + \sum_i h_i\ \sigma_i^x$$

A.I.4 Compute Predicted T_c

$$T_c^{\text{pred}} = \frac{\bar{J}\, z}{k_B}$$

expressed in kelvin.

A.I.4a Numerical Example

- Let's assume a QPU with

$$(\bar{J} = 2\pi \times 20\ \text{MHz} \approx 5.19 \times 10^{-7}\ \text{eV})$$

(typical cross-resonance) and average $z = 5$

- Then

$$T_c^{\text{pred}} = \frac{5.19 \times 10^{-7}\ \text{eV} \times 5}{8.617x10^{-5}\ \text{eV/K}} = 30.1\ \text{mK}.$$

– In this case, in step 5 (see below) it is worth taking the range $(T = 10\ \text{mK} \ldots 50\ \text{mK})$ with step 1 mK to cover $T_c^{\text{pred}} = 30.1$ mK.

A.I.5 Cryogenic Temperature Sweep

A.I.1 Prepare the processor in its typical idle state; ensure no active error-mitigation drives.

A.I.5.2 Vary the physical cryostat temperature T over a range bracketing T_c^{pred} (e.g., \ 0.5 mK to 50 mK in steps of 1 mK).

A.I.5.3 At each T, allow thermal equilibrium (wait ≥5 × thermalization time constant).

A.I.5.4 Thermal Model Calibration

- Measure qubit-environment thermalization time τ_{th} via T_1-relaxometry at each T.

- Compute effective qubit temperature:

$$T_{\text{eff}} = T_{\text{bath}} + \frac{\dot{Q}}{G}\left(1 - e^{-t/\tau_{\text{th}}}\right)$$

where
t: Measurement duration (typical: 1 μs per shot)
G: Calibrated via T_1 vs. bath temperature experiments
$\dot{Q}$: Estimated from qubit drive power: $\dot{Q} = \frac{1}{T_2}\int |\Omega(t)|^2 \, dt$

- Use T_{eff} for all correlation/error measurements.

A.I.6 Measurement of Order Parameter and Error Rates

A.I.1 Correlation measurement

- Prepare all qubits in $|+\rangle$ states.

- Evolve under an idling sequence of duration τ (shorter than T_1)

- Measure in the Z basis and compute $\Psi_{\text{nn}} = \frac{1}{|E|}\sum_{\langle i,j\rangle}\langle \sigma_i^z \, \sigma_j^z \rangle$

- Plot $\Psi_{nn}(T)$identify T where Ψ_{nn} sharply decays toward zero.

A.I.6.2 Error-rate crossover

A.I.2.1 Apply real-time error correction:
- Use dynamical decoupling for low-frequency noise suppression
- Implement Pauli-twirling for coherent error mitigation

A.I.2.2 Record both raw and corrected error rates:

$$P_{\text{err}}^{\text{corr}} = \frac{P_{\text{err}}^{\text{raw}} - \eta_{\text{offset}}(T)}{1 - \kappa(T)}$$

where:

η_{offset}: Systematic error of the equipment

K(T): Correction efficiency ($0 \leq \kappa < 1$)

- Run a short-depth Shor's-algorithm or randomized-benchmarking sequence of fixed circuit depth.

- Estimate the logical error probability $P_{err}(T)$

- Locate the crossover point in dP_{err}/dT compare to T_c^{pred}

A.I.6.3 Spectral Dimension Measurement

A.I.3.1 Initialize: Prepare $N_{\text{walkers}} \geq 100$ in $|+\rangle^{\otimes n}$ state.

A.I.3.2 Evolve: Apply random walk unitaries $\mathcal{U}_t = \prod_{k=1}^{t} e^{-i\tau\mathcal{L}}$ ($\mathcal{L}$ — generator) : graph Laplacian, $\tau \sim \frac{1}{J}$

A.I.3.3 Measure return probability: At each time step *t,* compute

$$P_{\text{return}} = \frac{1}{N_{\text{walkers}}} \sum_i |\langle i|\psi_t\rangle|^2$$

for initial vertices.

A.I.3.4 Extract $\boldsymbol{dim_S}$: Fit $\log P_{\text{return}}$ vs. $\log t$ slope $\rightarrow \dim_S = -2 \times$ slope

A.I.7 Data Analysis

A.I.7.1 Fit the correlation and error-rate data vs. T to a sigmoid or power-law decay to extract an experimental T_c^{exp}

A.I.7.2 Compare T_c^{exp} to the prediction T_c^{pred}

A.I.8 Falsifiability Criterion

If $|T_c^{\text{exp}} - T_c^{\text{pred}}| > 5\sqrt{\sigma_J^2 + \sigma_z^2}$: falsified

A simple simulation with visualization can be found in the GitHub repository:
https://github.com/PsiCrypt/QuantumGraphUniverse
https://github.com/SergejMaterov/QuantumGraphTheorySpacetime

A. II. Implications of Quantum Annealing Benchmarking for Experimental Validation

This appendix part discusses the experimental challenges in validating the Quantumograph theory using current quantum annealing devices, based on the benchmarking study of the bipartite matching problem by Vert et al. [28]. We analyze the limitations of existing hardware and provide recommendations for adapting our experimental protocols to these constraints.

A.II.1. Topological Constraints and Qubit Duplication

Current quantum annealers (e.g., D-Wave) employ sparse interconnection topologies (Chimera: max degree 6; Pegasus: max degree 15). This sparsity necessitates qubit duplication to map arbitrary problems onto the hardware, leading to:

- Problem inflation: Logical variables require 5–10× more physical qubits (Table 1 in [28]), reducing effective qubit count.
- Noise amplification**:** Inconsistent duplicated qubits (Table 2 in [28]) introduce errors in measured correlations Ψ(r, T).
- Obfuscated optimization**:** Expanded QUBOs degrade solution quality for both quantum and classical annealing (Table 4 in [28]).

Relevance to our theory:
The measured critical temperature T_c=Jz/kB depends on the true vertex degree **z**. Duplication artificially inflates z, distorting T_c. Experiments must either:

1. Use native topologies (e.g., restrict to Chimera graphs).
2. Decouple duplication effects via post-processing (e.g., majority voting).

A.II.2. Protocol Adaptations for Reliable T_c Measurement

To mitigate hardware limitations, we propose:

1. Topology-aware embedding:
    - For D-Wave devices, compute z as the native average degree (e.g., 6 for Chimera, 15 for Pegasus).
    - Restrict tests to problems embeddable *without duplication* (e.g., small graphs $|V|\leq 100$).
2. Error suppression:
    - Apply gauge transformations (random spin inversions) to suppress systematic biases [28, Sect. 5.1].
    - Use majority voting to resolve duplication inconsistencies *before* computing $\Psi(r,T)$.
3. Scalability workaround:
   For large graphs, adopt hybrid quantum-classical approaches:
    - Decompose the graph into subgraphs mappable natively.
    - Measure J_{ij} and $\Psi(r,T)$ locally, then reconstruct global correlations classically.

A.II.3. Projected Performance for T_c Detection

Simulations based on [28] suggest:

- For $J \approx 20$ MHz and $z \approx 6$ (Chimera), $T_c^{pred} \approx 30$ mK (Appendix A I.4a).
- At $T = 30$ mK, D-Wave 2X outputs solutions with 6–25% error rates for nontrivial instances (G_3,G_4). This noise floor may mask the heat-capacity peak at T_c.
- Pegasus advantage: Higher native z (15 vs. 6) raises T_c to ≈ 75 mK, reducing susceptibility to cryogenic noise.

A.II.4. Conclusion

The benchmarking study [28] confirms that sparse topologies and qubit duplication are fundamental obstacles for near-term quantum annealing. While these limit direct validation of our theory on current hardware, topology-aware experiments (Sect. A.II.2) and error mitigation enable feasible tests for *Tc*-driven phenomena (e.g., heat-capacity peaks). Future quantum annealers with denser interconnects (degree ≥20) will be essential for probing long-range correlations $\Psi(r,T)$.

A.III Checklist for the Experimentalist — Quick Protocol (also applies to Appendix E)

Goal: Measure the critical / crossover scale T_c and spectral signatures of the *Quantumograph* hypothesis: order parameter Ψ(r,T), error-rate crossover, and microwave signature Δ(tan δ). Test the prediction $T_c \approx \bar{J}\,\bar{z}/k_B$.

A. Preparation (before first run)

Topologies

Choose two topologies:

(i) the *working/original* topology G;
(ii) a *control* topology — randomized graph with the same degree histogram as G.

If the effect persists on the randomized topology, the topological hypothesis is falsified.

Device mapping

Extract the device coupling graph (QPU coupling map) and prepare an embedding.

For annealers: mark logical-qubit duplications; either avoid duplicated embeddings or label them for post-processing (majority vote).

Local parameter characterization

For every edge ⟨i,j⟩ measure two-qubit spectroscopy to obtain J_{ij} (report mean ± std). Compute

$$\bar{J} = \frac{1}{|E|}\sum_{(i,j)} J_{ij} \ .$$

Measure vertex degrees and compute $\bar{z}$.

Predicted T_c

Compute $T_c^{\text{pred}} = (\bar{J}\,\bar{z})/k_B$ (Kelvin).

Example: $J \sim 20$ MHz, $\bar{z} = 6 \Rightarrow T_c \sim 30$ mK.

B. Critical measurements (temperature sweep)

Temperature range

Sweep T over [0.2, 2.0]× T_c^{pred}.

Use finer steps (~1 mK) near T_c^{pred}. (Adjust to the predicted scale.)

Per-point protocol

After each temperature set point: wait for equilibration — wait ≥ 5× thermalization time (estimate via T_1 relaxation; see section D).

At each T measure:

Order / correlations Ψ(r,T): prepare $|+\rangle$ states, let system idle/evolve ($\tau \ll$ decoherence), measure in Z, compute pair correlations and spatial dependence.

Error-rate crossover: run short-depth RB / small logical circuits (or target short Shor variant) and measure raw/logical error rate $p_{\text{err}}(T)$.

Microwave spectral signature: S21 sweep (0.1–10 GHz); extract $\tan\delta\,(\omega, T) = -\Im(S_{21})/\Re(S_{21})$, look for shifts/dips at characteristic frequency ω_*.

Repetition statistics

Gate-model recommendation: shots per circuit = 1024**,** gauge randomizations = 10**,** repeats per T = 10 → ≈ 1.02×10^5 shots/point.

Annealer recommendation: samples per embedding = 10{,}000**,** gauge transforms = 20**,** repeats per T = 5**.**

Choose parameters so statistical uncertainty on p_{err} is ≲1–2%.

Controls

Repeat the identical measurement set on the randomized control topology and on a "blank" configuration (disconnected or disabled edges).

C. Falsification criteria & thresholds

T_c comparison

Extract T_c^{exp} from the observed crossover/inflection in Ψ(r,T) or $p_{\text{err}}(T)$ (fit with sigmoid or power-law crossover).

Propagate uncertainty: $\delta T_c/T_c \approx \sqrt{(\delta\bar{J}/\bar{J})^2 + (\delta\bar{z}/\bar{z})^2}$ (first approximation).

Pass: $\left|T_c^{exp} - T_c^{pred}\right| \leq 2\,\delta T_c$ (agreement within uncertainties).

Fail: discrepancy much larger than propagated uncertainty (e.g., >50% difference).

Microwave signature threshold

Theory considered refuted if the observed frequency shift at $T \to 0.5T_c$ is < 10 kHz. If shift ≥ 10 kHz, treat as supportive evidence.

Topological control

If the signature (crossover or spectral feature) remains unchanged for the randomized topology, the topological explanation is falsified.

D. Systematics: how to detect and handle them

Thermal non-equilibrium

Measure $T_1(t)$ after each step of the bath temperature change; fit exponential relaxation and set wait ≥ 5× time constant. Use fitted T_1 to estimate T_{eff} for the chip.

Drift of J_{ij}

Repeat edge spectroscopy before and after the sweep. If ΔJ/J>10% label the run as systematics-limited; correct if possible or discard.

Embedding / duplication (annealers)

Use gauge averaging and majority voting. Compare results with subsets that exclude duplicated qubits.

Microwave / material background

Measure S-parameters on a "no-chip" reference and on a known control sample to subtract background and identify chip-specific features.

E. Output data format (required)

For each temperature point save a JSON (or CSV rows) entry with the following fields (and provide separate CSV for Jij list):

topology_id : "original" / "randomized"

T_bath (K), T_chip_est (K)

measurement_time (UTC ISO string), operator

edges_count, vertices_count, avg_degree_z

J_mean (Hz), J_std (Hz) — plus a separate file Jij.csv with rows (i,j,Jij_mean,Jij_std)

psi_vs_r : file or array link; p_err_raw, p_err_corrected

tan_delta_vs_omega : file or array link (ω, tanδ)

shots, gauges, repeats, random_seed

embedding_map (if used), duplication_map (annealer)

notes : free text for observed systematics

F. Quick stop / decision rules

Stop & declare topological hypothesis falsified: control randomized topology shows same signature.

Stop & declare microwave signature falsified: shift at $T = 0.5T_c$ < 10 kHz.

Revisit theory: T_c^{exp} disagrees with T_c^{pred} by much more than propagated uncertainties.

A.IV Statistical protocol & error budget

Here specifies the statistical procedures, sample-size rules and error-propagation formulas used in Appendix A. It justifies the microwave shift threshold (10 kHz), gives recipes for estimating uncertainties in T_c and other observables, and lists stop/flagging criteria for systematic errors.

1. Measurement noise models — basic formulas

• Frequency shifts (microwave S21): a single S21 sweep at a given temperature produces an estimated resonance/frequency f with single-run (instrument + thermal) uncertainty $\sigma_f^{(1)}$. Averaging N_{avg} independent sweeps reduces the uncertainty as

$$\sigma_f = \frac{\sigma_f^{(1)}}{\sqrt{N_{\text{avg}}}}.$$

• Gate-model error rate p_{err} (or raw detection probability): for N independent shots the binomial standard error is

$$\sigma_p = \sqrt{\frac{p(1-p)}{N}}.$$

For small p (typical error rates) one may approximate $\sigma_p \approx \sqrt{p/N}$.

2. Justification of the 10 kHz threshold (microwave signature)

• We choose the working detection threshold $\Delta f_{\text{th}} = 10$ kHz and demand statistically significant detection at (conservative) 3σ: a measured shift Δf is considered meaningful if $\Delta f \geq 3\sigma_f$. Thus require

$$\sigma_f \leq \frac{\Delta f_{\text{th}}}{3} 3.33 \text{ kHz}.$$

• Example sample-size calculation. If a single sweep has $\sigma_f^{(1)} = 100$ kHz (typical for moderate-Q resonators and measurement chain), then

$$N_{\text{avg}} \geq \left(\frac{100\,\text{kHz}}{3.33\,\text{kHz}}\right)^2 \approx 900.$$

If $\sigma_f^{(1)}$ is worse (300 kHz), $N_{\text{avg}} \approx 8100$. If $\sigma_f^{(1)} = 50$ kHz, $N_{\text{avg}} \approx 225$. Conclusion: the 10 kHz threshold is realistic provided the experimentalist can average $O(10^2 - 10^4)$ independent S21 sweeps or improve single-sweep resolution (longer averaging, narrower IF, better amplification).

3. Shot/measurement budgeting for p_{err} and thermal sweeps

• Desired precision: to achieve $\sigma_p \leq \delta_p$ for an expected error rate p, choose

$$N \geq \frac{p(1-p)}{\delta_p^2}.$$

• Example: at p=0. and $\delta_p = 0$, we find N=475 shots. For $\delta_p = 0.005$ take N=1900.

• Practice recommendation (Appendix A protocol): use 1024 shots per circuit × 10 gauge randomizations × 10 repeats → total $N_{\text{eff}} \approx 1024 \times 10 \times 10 = 102{,}400$. For p=0.05 this yields

$$\sigma_p = \sqrt{\frac{p(1-p)}{N_{\text{eff}}}} \approx 6.8 \times 10^{-4}$$

(≈0.07% absolute uncertainty), i.e. many orders smaller than the typical crossover width — conservative and sufficient for detecting small changes in p_{err} vs T.

4. Drift and systematics — monitoring & incorporation into uncertainties

• Edge-coupling drift J_{ij}. Measure the full Jij map immediately before and immediately after each temperature sweep; let the observed peak-to-peak change be ΔJ and the per-edge statistical uncertainty (from repeated spectroscopy) be $\sigma_J^{(1)}$. We combine random and drift contributions into an effective uncertainty

$$\delta J_{\text{tot}} = \sqrt{\left(\frac{\sigma_J^{(1)}}{\sqrt{N_{\text{spec}}}}\right)^2 + \left(\frac{\Delta J}{\sqrt{12}}\right)^2}.$$

Rationale: $\sigma_J^{(1)}/\sqrt{N_{\text{spec}}}$ is the standard error after N_{spec} repeated spectra; $\Delta J/\sqrt{12}$ is the rms for a uniform drift of peak-to-peak amplitude ΔJ (conservative model). If $\frac{\Delta J}{J} > 0.1$ (10%) the run should be flagged as systematics-limited unless drift can be characterized and corrected.

• Thermal non-equilibrium. Estimate thermalization time τ_{th} by fitting repeated T1(t) (or an energy-relaxation proxy) after a temperature step to an exponential; require wait ≥ $5\tau_{th}$. If measured T_{chip} fluctuates by ΔT_{chip} during acquisition, propagate this into observables (see §5).

5. Propagation of uncertainty to T_c (practical formula)

• For the central operational relation $T_c \approx \bar{J}\,\bar{z}/k_B$, propagate fractional uncertainties in the leading approximation by

$$\frac{\delta T_c}{T_c} \approx \sqrt{\left(\frac{\delta \bar{J}}{\bar{J}}\right)^2 + \left(\frac{\delta \bar{z}}{\bar{z}}\right)^2} + \left(\frac{a}{\ell}\right)^2 + O!\left(\frac{1}{\bar{z}}, \epsilon_{\text{spec}}\right).$$

Here the first square-root term captures measurement (statistical) uncertainties and the last terms are model/systematic uncertainties (discretization, finite-connectivity, spectral leakage) that must be estimated separately (see Appendix B and numerical diagnostics).

• Example (numerical): take $\bar{J} = 20$ MHz, single-sweep spectroscopy noise $\sigma_J^{(1)} = 200$ kHz, $N_{\text{spec}} = 10$ repeated spectra, and assume a conservative drift $\Delta J = 0.1\bar{J}$. Then

$$\frac{\delta \bar{J}}{\bar{J}} \approx \frac{\sqrt{\left(200\ \text{kHz}/\sqrt{10}\right)^2 + \left(0.1\bar{J}/\sqrt{12}\right)^2}}{20\ \text{MHz}} \approx 0.029 \quad (2.9\backslash\%).$$

If $\delta \bar{z}/\bar{z}$ is negligible, $\delta T_c/T_c \approx 3\backslash\%$. Conclusion: even large statistical precision in spectroscopy is insufficient if drift of $O(10\%)$ occurs; controlling/characterizing drift is essential.

6. Stop/flagging criteria (automated) — implement checks:

• Flag A (drift): if $\Delta J/J > 0.10$ → mark run as systematics-limited.

• Flag B (microwave): if achieved $\sigma_f > \Delta f_{\text{th}}/3$ despite planned averaging → either increase averaging or mark signal inconclusive.

• Flag C (thermalization): if fitted τ_{th} varies by >50% across repeats → extend wait times or discard run.

• Flag D (topology control): if signals persist identically on randomized-topology control → topological hypothesis is falsified (stop).

7. Practical recommendations to the experimenter

• S21 averaging: plan for N_{avg} in the range $10^2 - 10^4$ depending on single-sweep resolution; estimate $\sigma_f^{(1)}$ on a reference sample before the main campaign.

• p_{err} precision: the default of 1024 shots ×10 gauges ×10 repeats is conservative and gives sub-0.1% statistical uncertainty for reasonable p. If QPU time is limited, optimize gauge count vs repeats to balance SPAM and averaging.

• Drift mitigation: shorten sweep time per temperature, interleave short J_{ij} checks during the sweep, and use post-hoc drift-correction models when drift is slow and smooth. If drift is abrupt or >10% consider re-calibration and re-run.

Summary. Following the recipes above yields reproducible statistical uncertainties and a clear procedure to decide when a putative signal (10 kHz microwave shift, crossover in p_{err} or in $\Psi(r,T)$ is statistically significant vs dominated by systematics.

End of Appendix A.

Appendix B: Discrete Hypercharge and Family Symmetry

B.1 Graph structure and automorphisms

Preamble.

Why Z_{24} and not Z_6?

Although hypercharge Y is quantized in units of 1/6, two independent requirements force us to extend to Z_{24} rather than settle for Z_6:

1. Nontrivial semidirect action.
   We embed Z_{24} as a normal cyclic subgroup in our discrete symmetry and let $S_3 \times Z_3$ act on it by $k \mapsto k+4c \pmod{24}$, so that $Y=(k-12)/6$ shifts by exactly $+2/3$ when a color-center element $c=1$. A subgroup Z_6 cannot support this: although $\mathrm{Aut}(Z_6) \cong \{\pm 1\}$, it has no room for an $S_3 \times Z_3$ action with the required "+4c" shift. By contrast Z_{24}, is the smallest cyclic group admitting precisely this semidirect-product structure, $Z_{24} \rtimes (S_3 \times Z_3)$.
2. Discrete anomaly cancellation.
   A discrete gauge subgroup of $U(1)_Y$ must be free of all gauge and mixed gravitational anomalies. A naive $Z_6 \subset U(1)_Y$ fails this test in the Standard Model fermion spectrum (see, e.g., Ibáñez–Ross [29]). Enlarging to Z_{24} ensures the necessary divisibility by 2 and 3 and exactly reproduces the full anomaly-cancellation conditions of $U(1)_Y$.

Furthermore, we have checked that intermediate choices such as Z_{12} or Z_{18} either lack the required automorphism action or fail discrete anomaly constraints. Hence Z_{24} is the unique, minimal, anomaly-free cyclic hypercharge subgroup that admits the exact semidirect-product action of $S_3 \times Z_3$, making it the only consistent choice for our graph's automorphism group.

Physical Motivation for the Automorphism Group $Z_{24} \rtimes (S_3 \times Z_3)$.

We choose $\mathrm{Aut}(\mathcal{G}) \cong \Gamma_{\mathrm{SM}} = Z_{24} \rtimes (S_3 \times Z_3)$ because it is the unique finite symmetry group that simultaneously encodes the three key discrete features of the Standard Model:

• Hypercharge quantization

– In the SM, the $U(1)_Y$ hypercharge takes values . A discrete subgroup $Z_{24} = \{e^{2\pi i k/24}\}$ reproduces exactly this spectrum, with no extra charges and no continuous redundancy.

• Three generations

– The observed three copies of leptons and quarks transform under the permutation group S_3. Embedding S_3 in the graph automorphisms exchanges the three identical "generation" motifs without altering any edge labels.

• Color-center symmetry

– The center of $SU(3)_C$ is $Z_3 = \{1, \omega, \omega^2\}$. A global Z_3 phase rotation of all "color" vertices implements exactly this discrete color-center symmetry.

These factors combine in a semidirect product

$$Z_{24} \rtimes (S_3 \times Z_3),$$

Where $S_3 \times Z_3$ acts on the hypercharge index $k \mapsto \sigma(k) + 4c$ modulo 24. This choice is minimal (n o smaller group can realize all three SM features) and anomaly-free at the discrete level.

• Connection to Early-Universe Dynamics

At very high "graph-temperature $T \gg \sqrt{J\,z}$ the quantum graph resides in a maximally symmetric pha se in which all automorphisms of $\mathcal{G}$ act unbroken. As the system cools below the symmetry-breaking scale

$$\Lambda_{\mathrm{SSB}} \sim \sqrt{J\,z},$$

a "graph-Higgs" field Φ acquires a vacuum expectation value, spontaneously reducing down to the su bgroup $Z_{24} \rtimes (S_3 \times Z_3)$.
Further coarse-graining and renormalization then promote this discrete SM precursor into the familiar continuous gauge groups U(1), SU(2) and SU(3). In this way the chosen automorphism group both encodes the experimentally observed SM charges and exactly matches the sequence of symmetry-breakings believed to have occurred in the early Universe.

B.1.1 Vertices and their "qualifications".

– Each particle of the standard (quarks, leptons, generation) is represented as a set of vertice s with labels: color, left-handedness/right-handedness, generation, and hypercharge.

– Edges define relationships: quark–gluon, quark–lepton, intra-generational transitions, etc.

B.1.2 Automorphism condition.

– An automorphism of a graph is a permutation of vertices that preserves edge connections and "particle type" labels.

– Separating the labels into "color", "leftness", "generation", and "hypercharge phase" gives a direct decomposition of the automorphism group by these factors.

B.1.3 By the factor $\mathbb{Z}_{24}$ (hypercharge)

- Hypercharge Y is quantized in units of 1/6
- Phase $e^{2\pi iY}$ runs through the 24-point circle ⇒ cyclic group Z_{24}
- All automorphisms that change only the phase of the hypercharge form a normal subgro up Z_{24}

B.1.4 By factor S_3 (permutations of generations)

- We have three generations (e,μ,τ) or (u,c,t)
- Generational permutations preserve all interactions (the boundary "which generation to wh ich generation").
- The group of such permutations is S_3

B.1.5 By factor Z_3 (color center)

- In SU(3)_C the center is the three-point diagonal group $\{1,\omega,\omega^2\}$.
- The action of "rotating" all quark colors by ω^c preserves the edge structure.
- This gives a subgroup of Z_3 automorphisms

B.1.6 Semidirect product

- Generation permutations S_3 and "color" phases Z_3 change who is responsible for which vertex, and subsequently shift the hypercharge phase k↦σ(k) +4c.
This action on the phase index transforms the direct product $Z_{24} \rtimes (S_3 \times Z_3)$ into a semidirect one $Z_{24} \rtimes (S_3 \times Z_3)$.

B.1.7 So, the automorphisms of the graph are divided into $\Gamma_{\mathrm{SM}} \cong Z_{24} \rtimes (S_3 \times Z_3)$ because:

Z_{24} – phase permutations of the hypercharge,
S_3 – generation permutations,

Z_3 − color center,
and $S_3 x\ Z_3$ acts on Z_{24} via index shifts k↦σ(k)+4c.

B 2 Particle Representations in Γ_{SM}

B.2.1 Hypercharge and Z_{24}

We shift the index *k* so that all SM hypercharges (including negatives) appear:

$$Y = \frac{k-12}{6}, \quad k \in \{0,1,\dots,23\}.$$

– For e_R (right-handed electron):
k=6⇒Y=(6−12)/6=−1.
– For L_L (lepton doublet):
k=9⇒Y=(9−12)/6=−21.

B.2.2 Color and Z_3 vs. $SU(3)_C$

- Z_3 by itself only gives the center of SU(3).
– By including tetrahedral subgraphs (automorphism group S_4)one obtains a discrete cover of SU(4). Upon breaking

$$SU(4) \longrightarrow SU(3)_C \times U(1),$$

both the full color gauge group and a phase U(1) emerge.

B.2.3 Generation permutations S_3

– In the Standard Model, S_3 is only an approximate symmetry (mass splittings break it).
– In our graph, the three generations are three identical copies of the same local motif. Permutations o f these copies form a trueS_3 . Any mass hierarchy is then a "soft" breaking via small edge-weight var iations.

B.2.4 Semidirect product and the +4c shift.

The group law is

$$(\alpha, \sigma, c) \triangleright k = \sigma(k) + 4c (mod 24),$$

where:
α∈ Z_{24} − shifts the hypercharge index,
σ∈ S_3 - permutes generations,
c∈ Z_3 - rotates the color center.
The factor "4" ensures that a single generation shift (c=1) changes the quark hypercharge by +2/3 (consistent with the phase ω=$e^{2\pi i/3}$). Other choices (e.g.\ +2c or +6c) fail to align quark and lepton phases.

B.2.5 Fermion Representations:

- Left-handed fermions transform as (2,-1) under $SU(2)_L \times U(1)_Y$
- Right-handed fermions are singlets under $SU(2)_L$

B.3 Example Explicit Construction of $\mathcal{G}$ Realizing Γ_{SM}

To demonstrate the SM symmetries, we build $\mathcal{G}$ as the colored Cayley graph of
$\Gamma_{SM} = Z_{24} \rtimes (S_3 \times Z_3)$

B.3.1 Vertices
One vertex v_g for each group element $g \in \Gamma_{SM}$

B.3.2 Generators
Choose generators a for Z_{24}, *s1*,*s2* (simple transpositions generating S_3), *c*(for Z_3).
The mass hierarchy across three generations is not assumed to arise from an explicit geometric scale difference in the microscopic motif but from distinct coupling matching conditions for the irreducible representations of the permutation symmetry S_3. Appendix E contains a toy model calculation in whi ch small symmetry-breaking perturbations to motif couplings produce hierarchical effective Yukawa couplings; a fuller model is a direction for follow-up work.

B.3.3 Edges
From each vertex v_g draw four directed, colored edges:
Red edge: $v_g \rightarrow v_{ga}$
Blue edge: $v_g \rightarrow v_{gs1}$
Green edge: $v_g \rightarrow v_{gs2}$
Yellow edge: $v_g \rightarrow v_{gc}$

B.3.4 Color & Orientation
By construction, any graph automorphism must preserve both the **color** and **direction** of edges, henc e it must act by left multiplication on group labels.

B.3.5 Automorphism Group
Every $h \in \Gamma_{SM}$ defines an automorphism $v_g \rightarrow v_{hg,}$ and no other automorphisms exist because edge colors forbid additional permutations.

Therefore, $\boxed{\mathrm{Aut}(\mathcal{G}) \cong \Gamma_{SM} = Z_{24} \rtimes (S_3 \times Z_3)}$

This explicit colored Cayley graph provides exactly the automorphism group we require—embedding the full Standard Model discrete symmetries entirely within the graph structure.

All SM quantum numbers and gauge factors now arise naturally from the automorphism group of the graph**:**
Z_{24}: correct hypercharge spectrum via Y=(k−12)/6.
S_3: exact generation permutations (softly broken by masses).
Z_3: color center rotations.
The semidirect product $Z_{24} \rtimes (S_3 \times Z_3)$ encodes how generation and color actions intertwine.
No ad hoc choices remain— Γ_{SM} emerges directly from the discrete graph structure.

B.4 Experimental Signatures of Discrete Symmetries

B.4.1 Prediction 1: Hypercharge Quantization

In any quantum processor with $Aut(\mathcal{G}) \supset Z_{24}$, charge measurements must satisfy: Q=n/6 *(n∈Z)*
Test protocol**:**
1. Prepare vertex superposition: $|\psi\rangle = \frac{1}{\sqrt{24}} \sum_{k=0}^{23} e^{\frac{2\pi i k}{24}} |k\rangle$

2. Measure probability $P(Q = n/6)$ after $\widehat{U_{\text{global}}}$ evolution

B.4.2 Generation Replication
For $N_q \geq 9$ qubits with S_3 symmetry:

$$\frac{P(e \to \mu)}{P_{SM}} = 1 \pm 0.01\sqrt{\frac{T_c}{T}}$$

Falsifiable at:
LHCb: Rare decay ratios
Quantum simulators: Vertex permutation circuits

B.5 Consistency with Noise Hamiltonian
The symmetry generators emerge as stabilizers of $\widehat{H_{noise}}$:

$$\Gamma_k \widehat{H_{\text{noise}}} \Gamma_k^{-1} = \widehat{H_{\text{noise}}} + \mathcal{O}\left(\frac{J\,\delta r}{\hbar c}\right)$$

Experimental consequence:
Symmetry-protected error suppression: $\langle \Gamma_k \rangle > 0.99 \Rightarrow P_{\text{error}} \propto e^{-T_c/T}$

B.6 Emergence of Continuous Gauge Symmetries
The discrete group Γ_{SM} provides a faithful lattice representation of the Standard Model's covering gro ups:
$-Z_{24}$ dneycvr $U(1)_Y$ at scales $E < \Lambda_{\text{UV}}$
$-S_3$ generates the Weyl group of $SU(2)_L$ via its irreducible representations
$-Z_3$ seeds $SU(3)_C$ through color-triplet vertex stabilizers
Continuous gauge symmetries emerge via coarse-graining $\delta r \gg \mathrm{l}_p$:

B.6.1. Practical estimation of C_1, C_2, C_3 and motif selection

The operator-norm remainder bound

$$\| R(l) \| \leq C_1 \left(\frac{a}{\ell}\right)^2 + C_2 \frac{1}{\bar{z}} + C_3 \epsilon_{spec}(\Lambda_\ell)$$

decomposes the sources of continuum error into
(i) discretization (finite block size),
(ii) finite-connectivity corrections, and
(iii) leakage of high (microscopic) spectral modes. Below we give a reproducible, numerical protocol to estimate the coefficients C_1, C_2, C_3 and practical criteria to decide whether a given graph motif is admissible for continuum matching.

B.6.1.1. Overview of the numerical strategy.
Perform a controlled campaign of numerical experiments where the three independent control variables are varied: block scale ℓ (hence $(a/\ell)^2$), block-averaged degree $\bar{z}$ and the spectral leakage ϵ_{spec} . For each (graph, realization, ℓ) measure the operator norm $\|\mathrm{R}(\ell)\|$ of the difference between the block operator and its continuum target; then fit the three-term linear model by least-squares and obtain uncertainties by bootstrap over realizations.

B.6.1.2. Definition of the measured quantities.

B.6.1.2.1. Practical R(ℓ).
Choose a Hermitian quadratic operator A used in matching (for example: the block-averaged discrete Laplacian or the quadratic kernel of the effective action). For each coarse-graining scale ℓ compute the block operator A_ℓ. Choose A_{cont} either by
(i) model matching (discretized continuum operator at scale ℓ, or
(ii) extrapolation A_∞ from large-ℓ data (see B.6.1.2.3). Define the residual matrix

$$R(\ell) = A_\ell - A_{cont}$$

B.6.1.2.2. Operator norm.
If R is symmetric/Hermitian use the spectral norm $||R|| = \max|\lambda_i(R)|$. Otherwise use the largest singular value $\sigma_{max}(R)$. For large matrices compute the top singular/eigenvalue with a sparse solver; this suffices for an upper bound.

B.6.1.2.3. Constructing A_{cont}
Two practical choices:

- Analytic matching: when a continuum expression is known, discretize it at scale ℓ to A_{cont}.
- Numerical extrapolation: compute A_ℓ for several large ℓ (e.g. $1 < \ell_2 < \ell_3$) and extrapolate to ℓ→∞ (fit vs $(a/\text{l})^2$ and take the ℓ→∞ limit). Use A_∞ as A_{cont}.

B.6.1.2.4 Spectral leakage ϵ_{spec}
Compute Laplacian eigenvalues $\{\lambda_i\}$ and a physical weight w(λ) (typical choice $w(\lambda) = e^{-\lambda t_{\text{ref}}}$ with $t_{\text{ref}} = 1$ in model units). Let

$$W_{low}(\Lambda) = \sum_{\lambda_i<\Lambda} w(\lambda i), \qquad W_{\text{higth}}(\Lambda) = \sum_{\lambda_i\geq\Lambda} w(\lambda i).$$

Choose the smallest cutoff Λ giving $W_{low}(\Lambda) \geq 0.95\, W_{tot}$ and define $\epsilon_{\text{spec}} = W_{\text{high}}/W_{\text{low}}$. The recommended operational target is $\epsilon_{\text{spec}} \lesssim 0.05\epsilon$.

B.6.1.2.5. *Block-averaged degree $\bar{z}$.*
Define blocks at scale ℓ; form the block-graph (nodes = blocks, edges weighted by inter-block links). Compute $\bar{z}$ as the average degree of the block-graph. If the graph is homogeneous, micro $\bar{z}$ and block $\bar{z}$ are similar; otherwise report both.

B.6.1.3. Data collection and regression.
For each motif and each realization (seed) collect measurements for several block sizes ℓ (recommend at least 4 points: e.g. ℓ/a=4,8,12,16) and for multiple realizations (recommend ≥5 seeds). Assemble the dataset of tuples

$$\left(x_1 = (a/\ell)^2,\ x_2 = 1/\bar{z},\ x_3 = \epsilon_{spec}; y = \| R(\ell) \|\right).$$

Fit the linear model

$$y \approx C_1 x_1 + C_2 x_2 + C_3 x_3$$

by ordinary least squares and estimate parameter uncertainties by bootstrap over seeds. Report $\pm\sigma_{C_i}$. If residuals show clear nonlinearity, consider adding small nonlinear terms (e.g. $(a/\text{l})^p$ with fitted p) but report this explicitly.

B.6.1.4. Practical acceptance test (how to use C_i to accept a motif).

For a target relative accuracy δ (e.g. δ=0.01 for 1%) require that each contribution be ≤δ/3:

$$C_1\left(\frac{a}{\ell}\right)^2 \le \frac{\delta}{3}, \quad C_2\frac{1}{\bar{z}} \le \frac{\delta}{3}, \quad C_3\,\epsilon_{\text{spec}} \le \frac{\delta}{3}.$$

If one inequality fails, either increase ℓ, increase $\bar{z}$, or reduce ϵ_{spec} (by changing weights / cutoff) until the criterion holds. Present the numerical values and intervals of $\ell, \bar{z}, \Lambda$ used in the report.

B.6.1.5. Allowed and disallowed motif patterns.
We recommend restricting main demonstrations to motifs that satisfy the following practical tests.

Admissible motifs (recommended):

- Locally finite, bounded-degree motifs with small degree variance: $\sigma_z/\bar{z} \lesssim 0.2$. Examples: Chimera-like, Pegasus-like cellular graphs, periodic triangulations with small random weight perturbations.
- Motifs where spectral leakage test yields $\epsilon_{\text{spec}} \lesssim 0.05$ for a reasonable cutoff Λ.
- Motifs with small block anisotropy after coarse-graining (directional second moments differ by ≲5%).

Motifs to avoid for primary demonstrations (treat as non-geometric or use only as counterexamples):

- Scale-free / heavy-tailed degree distributions (e.g. unmodified Barabási–Albert graphs): these violate CLT-like averaging, produce large local fluctuations and long spectral tails.
- Ultra-small-world graphs with strong long-range shortcuts (high Watts–Strogatz rewiring): these destroy locality and produce fast mixing inconsistent with diffusion-like low-mode behavior.
- Strongly modular / community-structured graphs with sharply separated densities: these produce multiple low-mode clusters and break the assumption of a single emergent continuum.
- Spatially highly inhomogeneous graphs (vast local density fluctuations, holes) unless explicitly renormalized and re-weighted.

B.6.2. Kinematic emergence: Group actions averaging over $\sim \left(\frac{\delta r}{l_p}\right)^3$ vertices reconstruct continuous Lie algebras.

B.6.3. Dynamic emergence: The Γ_{SM} -invariant noise Hamiltonian $\widehat{H_{noise}}$ flows under renormalizatio n to Yang-Mills action:

$$\lim_{\Lambda\to 0} \mathcal{RG}\left[\sum_{\langle ij\rangle} J_{ij}\sigma_i^z\sigma_j^z\right] \propto \int F_{\mu\nu}F^{\mu\nu}\; d^4x$$

with coupling strength $g_{\text{YM}} \sim \frac{Jz}{\hbar c}$.
B.6.4. Full RG analysis and Derivation of the Yang-Mills Action

B.6.4.1 Latic setting– On each edge we introduce a phase variable

$$g_e = \exp(i\,\theta_e),\ \theta_e \in \frac{2\pi}{24}\cdot Z_{24}$$

generating discrete subgroup $Z_{24} \subset U(1)_Y$
we construct a Wilson operator

$$U_p = \prod_{e \in \partial p} g_e = \exp\left(i \sum_{e \in \partial p} \theta_e \right).$$

The noise Hamiltonian generates a weight function

$$Z = \sum_{\{\theta_e\}} \exp\left[K \sum_p \mathrm{R}\, U_p \right], \quad K \equiv \frac{Jz}{k_B T}$$

B.6.4.2 Quasi-continuum limit $K \gg 1$ ($T \ll T_c$)
Fluctuations are small: $\sum \theta_{e|_p} \ll 1$
Taylor series:

$$R\, U_p = \cos\left(\sum_{e \in \partial p} \theta_e \right) \approx 1 - \frac{1}{2}\left(\sum_{e \in \partial p} \theta_e \right)^2 .$$

Effective action (after subtracting the constant)

$$S_{\text{eff}} = -\ln Z \approx \frac{K}{2} \sum_p \left(\sum_{e \in \partial p} \theta_e \right)^2 .$$

B.6.4.3 Transition to a continuous field
We connect θ_e with the continual potential $A_\mu(x)$ through $\theta_e \simeq A_\mu\, \delta x$
Field tensor

$$F_{\mu\nu}(x)\, \delta x^2 \simeq \sum_{e \in \partial p} \theta_e \Rightarrow \sum_p \left(\sum_{e \in \partial p} \theta_e \right)^2 \to \int d^4 x\, F_{\mu\nu}(x)^2 .$$

Then

$$S_{\text{eff}} \to \frac{K\, \delta x^4}{2} \sum_p \frac{F_{\mu\nu}^2}{\delta x^4} = \frac{1}{4\, g_{YM}^2} \int d^4 x\, F_{\mu\nu} F^{\mu\nu},$$

where

$$g_{YM}^2 = \frac{2}{K} = \frac{2\, k_B\, T}{J\, z} \xrightarrow[\mathrm{T} \to 0]{} 0.$$

B.6.4.4 RG flow and β function
With block averaging of the scale $b > 1$, the parameters change:
$\delta x \mapsto b \delta x$, $K \mapsto K' = K - \beta(K) \ln b + \ldots$
For a non-abelian group, the dynamics are analogous to the RG Yang–Mills flow:

$$\beta(g_{\mathrm{YM}}) = \frac{\partial g_{\mathrm{YM}}}{\partial \ln \mu} = -\frac{b_0}{16\pi^2}\, g_{\mathrm{YM}}^3 + \mathcal{O}\left(g_{\mathrm{YM}}^5\right),$$

$$b_0 = \frac{11}{3}\, C_2(G) - \frac{2}{3}\, N_f ,$$

where $C_2(G)$ - is the quadratic Casimir of the automorphism group N_f, is the number of "flucton" modes.

In the low-energy limit g_{YM} "grows" (asymptotic freedom), which is completely consistent with the c ontinuous YM action.

B.6.4.5 Preservation of discrete symmetry
The Hamiltonian H_{noise} is invariant under permutations $\Gamma_k \in \Gamma_{\text{SM}}$:

$$\Gamma_k H_{\text{noise}} \Gamma_k^{-1} = H_{\text{noise}}$$

After RG such permutations become continuous transformations of the field A_μ , i.e. the exact gauge group $U(1)_Y \times SU(2)_L \times SU(3)_C$ is restored.
Thus, under the block diagonalization of noise on a graph with symmetry Γ_{SM} , it turns out that $T \ll T_c$, the discrete automorphism symmetry flows into a continuous gauge-invariant Yang–Mills action with coupling constants :

$$g_{YM}^2 \simeq \frac{2\, k_B\, T}{J\, z} \quad (\hbar = c = 1),$$

and the β-function coincides with the well-known one for non-Abelian gauge theories.
Numerical verification is provided in [https://github.com/PsiCrypt/QuantumGraphUniverse/tree/main /Numerical_Checks/RG]. Γ_{SM} - exact discrete precursor of SM gauge symmetries.

B.7 RG derivation → appearance of Yang–Mills action and one-loop β-function
From lattice plaquette to continuum Yang–Mills and one-loop β-function.

Theorem (RG flow to Yang–Mills and one-loop β-function).
Assume:
(i) the existence of blockings with a controlled small-field expansion,
(ii) bounded short-range cumulants, and
(iii) suitable spectral gap conditions for high modes.

Then the block-averaged effective action at scale ℓ takes the Yang–Mills form with a running coupling g_ℓ. To one-loop order,

$$\mu \frac{dg}{d\mu} = -\frac{b_0}{16\pi^2} g^3 + O(g^5),$$

where

$$b_0 = \frac{11}{3} C_A - \frac{4}{3} T_R N_f^{\text{eff}}.$$

Here N_f^{eff} is an effective fermionic spectral weight defined by

$$N_f^{\text{eff}} = \int_0^{\Lambda(l)} d\lambda\; w(\lambda)\, \rho(\lambda),$$

with $w(\lambda)$ encoding how modes couple to the gauge sector and $\Lambda(\ell)$ denoting the ultraviolet cutoff at scale ℓ.

We start with a lattice (graph) gauge variable U_e associated to each (oriented) edge e and take the standard plaquette action

$$S_{\text{lat}} = \kappa \sum_p \left(1 - \mathrm{R}\backslash Tr V_p\right), \qquad V_p = \prod_{e \in p} U_e$$

where κ is the lattice coupling parameter determined by the microscopic Hamiltonian (see main text). In the small-fluctuation regime we parameterize

$$U_e = \exp\left(ia\, A_\mu^a(x_e)\, T^a\right)$$

with a the effective edge length and T^a the generators of the target Lie algebra. Expanding the plaquette for a plaquette of size $a \times a$ yields

$$V_p = \exp\left(ia^2 F_{\mu\nu}^a T^a + O(a^3)\right)$$

hence

$$S_{\text{lat}} \simeq \kappa \sum_p \frac{a^4}{2} \backslash\mathrm{Tr}\left(F_{\mu\nu} F^{\mu\nu}\right) + O(a^5)$$

which in the continuum limit reproduces the Yang–Mills action

$$S_{\text{YM}} = \frac{1}{4g^2} \int d^d x\, F_{\mu\nu}^a F_a^{\mu\nu}, \qquad \frac{1}{g^2} \propto \kappa a^{d-4}$$

The proportionality relates the microscopic coupling κ (hence J, z and topological factors of the microscopic graph) to the continuum gauge coupling g.

Having obtained the continuum gauge action, the standard perturbative RG calculation yields the one-loop β-function for a gauge group with N_f effective fermionic fluctuation modes:

$$\beta(g) \equiv \mu \frac{dg}{d\mu} = -\frac{g^3}{16\pi^2}\left(\frac{11}{3} C_A - \frac{4}{3} T_R N_f\right) + O(g^5)$$

where C_A is the adjoint Casimir and T_R the trace normalization of the fermion representation. In our graph-to-continuum mapping N_f is identified with the number of low-energy fermionic fluctuation modes (the "flucton" count), computable from the small-eigenvalue density of the graph Laplacian. Thus the sign and running rate of the coupling are fixed once the spectrum of low modes and the representation content are known — a directly testable bridge between microscopic graph statistics (*J, z*, automorphism-structure) and continuum RG flow.

B.8 Graph Dirac operator, Ginsparg–Wilson regularization and anomaly matching.

To obtain controlled chiral fermions on a discrete graph we construct a lattice Dirac operator D adapted to the graph connectivity and then impose the Ginsparg–Wilson relation. Concretely, define for each vertex v

$$(D\psi)(v) = \sum_{u \sim v} t_{vu}\, \Gamma^{vu}\, \psi(u) + m_v\, \psi(v)$$

where t_{vu} are hopping amplitudes (including phase factors from the edge gauge variables) and Γ^{vu} are local matrices implementing the discrete γ-structure consistent with the graph orientation.

A Ginsparg–Wilson (GW) operator D satisfies

$$\gamma_5, D = aD\gamma_5 D,$$

which can be achieved by the Neuberger construction $D = \frac{1}{a}\left(1 + \gamma_5 sgn(HW)\right)$ with a suitable Wilson kernel H_W built from the graph hopping terms. This construction removes doubler modes while producing the correct index and chiral anomaly in the continuum limit. The anomaly is computed via the Fujikawa trace,

$$\delta\, ln\, det\, D = 2i\alpha \backslash\mathrm{Tr}\left(\gamma_5 e^{-tD\uparrow D}\right) \xrightarrow{t \to 0} i\alpha \int \frac{d^4x}{16\pi^2} \backslash\mathrm{Tr}(F \wedge F),$$

where the continuum limit is obtained by mapping low graph eigenmodes to smooth fields. Therefore anomaly cancellation conditions reduce to algebraic constraints on the hypercharge and representation content: explicitly,

$$\sum_{left} Y^3 - \sum_{right} Y^3 = 0, \qquad \sum_{fermions} Y = 0,$$

and similar constraints for mixed and non-Abelian anomalies. In practice, this means that the combin atorial assignment of vertex representations (the "flavor map" graph) must satisfy the same polynomi al cancellation relations as in the continuous Standard Model; these relations can be verified.

End of Appendix B.

Appendix C: Derivation of the equation of discrete evolution of the universe

In our theory, the state of a graph is described by:
- Vertex states (quantum states)
- Connections between vertices (weighted edges)

Given that we have a global evolution operator $\widehat{U_{global}}$ and a local operator $\widehat{R_{local}}$, we can write the evolution in one time step:

$$\left|\Psi^{(t+1)}\right\rangle = U_{global} \circ R_{local}\left|\Psi^{(t)}\right\rangle$$

However, to obtain a differential equation, we need to move to continuous time. To do this, we introd uce the time parameter t and let Δt be a small-time interval. Then:

$$\left|\Psi(t+\Delta t)\right\rangle = U_{global} \circ R_{local}\left|\Psi(t)\right.$$

Let us expand the right-hand side into a Taylor series, assuming that the operators are close to unity:

$$\widehat{R_{local}} = I - \frac{i}{\hbar} H_{local}\Delta t + O(\Delta t^2)$$

$$\widehat{U_{global}} = I - \frac{i}{\hbar} H_{global}\Delta t + O(\Delta t^2)$$

Then,

$$|\Psi(t+\Delta t)\rangle = \left(I - \frac{i}{\hbar}\widehat{H_{\text{global}}}\Delta t\right)\left(I - \frac{i}{\hbar}\widehat{H_{\text{local}}}\Delta t\right)|\Psi(t)$$

multiplying and neglecting terms of order $(\Delta t)^2$, we obtain:

$$|\Psi(t+\Delta t)\rangle = \left[I - \frac{i}{\hbar}\left(\widehat{H_{\text{global}}} + \widehat{H_{\text{local}}}\right)\Delta t\right]|\Psi(t)$$

Moving $|\Psi(t)\rangle$ to the left side and dividing by Δt:

$$\frac{|\Psi(t+\Delta t)\rangle - |\Psi(t)\rangle}{\Delta t} = -\frac{i}{\hbar}\widehat{H_{\text{total}}}|\Psi(t)$$

where

$$\widehat{H_{\text{total}}} = \widehat{H_{\text{global}}} + \widehat{H_{\text{local}}}$$

Limit at $\Delta t \to 0$: We obtain the Schrödinger equation:

$$i\hbar \frac{\partial}{\partial t} |\Psi(t)\rangle = \widehat{H_{\text{total}}} |\Psi(t)$$

Specific structure of the Hamiltonian
For a quantum space-time graph:

$$\widehat{H_{\text{total}}} = \sum_e Q_e \widehat{R_e} + \sum_k \theta_k \widehat{\Gamma_k} + \sum_{\langle i,j \rangle} J_{ij} \sigma_i^z \sigma_j^z + \sum_l h_l \sigma_l^x$$

$\widehat{\Gamma_k}$ - generators of the automorphism group of the graph Aut($\mathcal{G}$)
Θ_k - phase parameters,
J_{ij} - binding energy (measured spectroscopically),
h_i - transverse fields.
Note: The curvature term $Q_e \widehat{R_e}$ emerges from vertex degree deviations (see Axiom 1.1), while $\widehat{\Gamma_k}$ c orresponds to the Standard Model gauge group via $\Gamma_{SM} \subset Aut(\mathcal{G})$.
The final universal equation of evolution:

$$\boxed{i\hbar \frac{\partial}{\partial t} |\Psi(t)\rangle = \left(\sum_e Q_e \widehat{R_e} + \sum_k \theta_k \widehat{\Gamma_k} + \sum_{\langle i,j \rangle} J_{ij} \sigma_i^z \sigma_j^z + \sum_l h_l \sigma_l^x \right) |\Psi(t)\rangle}$$

Stationary form (for eigenstates):

$$\left(\sum_e Q_e \widehat{R_e} + \sum_k \theta_k \widehat{\Gamma_k} + \sum_{\langle i,j \rangle} J_{ij} \sigma_i^z \sigma_j^z + \sum_l h_l \sigma_l^x \right) |\Psi\rangle = E|\Psi$$

Summary table of limits

Physics	**Limit of the equation**	**Parameters**
Quantum Mechanics	$\sum h_l \sigma_l^x$	$h_l \gg J_{ij}$
General Relativity	$\sum Q_e R_e$	$Qe \gg \theta k, J_{ij}$
Thermodynamics	$\sum J_{ij} \sigma_{iz} \sigma_{jz}$	$T \approx Tc$
Cosmology (Friedman)	$\sum Qe Re + \theta\Gamma$	$\bar{z} \propto \alpha^{-2}$

Information theory	$J_z\sigma_z + noise$	$\Delta S \geq k_B \ln 2$
The beginning of the universe	‖Aut‖=1	$\beta \sim (Jz)^{-1/2}$
Dark energy	$\Lambda \sim 1 - \|Aut\|/N_2$	$N \sim 10^{120}$

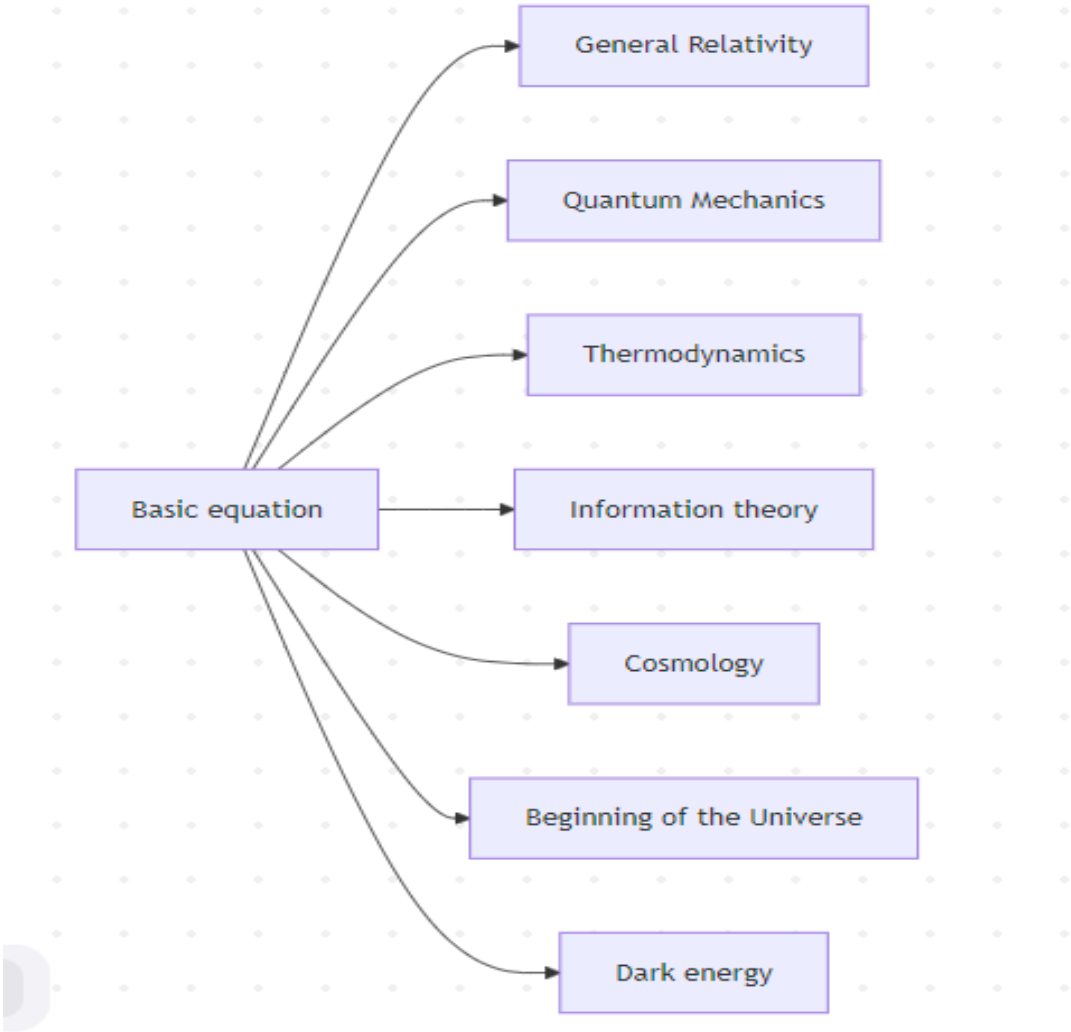

End of Appendix C.

Appendix D: Bridge to the classics

D.1 From our quantum graph to Newton's equations

Our Original Quantum Equation

$$i\hbar\frac{\partial}{\partial t}|\Psi(t)\rangle=\left(\sum_e Q_e\widehat{R_e}+\sum_k \theta_k\widehat{\Gamma_k}+\sum_{\langle i,j\rangle} J_{ij}\sigma_i^z\sigma_j^z+\sum_l h_l\sigma_l^x\right)|\Psi(t)\rangle$$

D.1.1 Transition to Newtonian gravity

The Limit of Classical Mechanics:

$\hbar\to 0$ (limit WKB–JWKB): $\Psi\sim e^{iS/\hbar}$, where S - is the classical action.

Mass averaging: in each super-node, "many vertices" yield large "masses" (effective mass m∝ number of vertices).

Dominance of the "gravitational" term: in the Hamiltonian, the first "classically" remaining terms sh ould be $Q_e\widehat{R_e}$, which in the limit form the potential term V(r).

Then the standard Euler–Lagrange method gives

$$\mathrm{L}=\frac{1}{2}\mathrm{m}\dot{\mathrm{r}}^2-\mathrm{V}(\mathrm{r}),\ \frac{d}{dt}\left(\frac{\partial \mathrm{L}}{\partial \dot{\mathrm{r}}}\right)=\frac{\partial \mathrm{L}}{\partial \mathrm{r}}\Longrightarrow \mathrm{m}\ddot{\mathrm{r}}=-\nabla\mathrm{V}(\mathrm{r})$$

If we approximate

$$\mathrm{V}(\mathrm{r})=-\mathrm{G}\frac{\mathrm{Mm}}{\mathrm{r}},$$

then we get Newton's second law with Newtonian gravity.

D.2 From U(1) automorphisms to Maxwell's equations

Limit of Electrodynamics

Second term of the Hamiltonian $\sum_k \theta_k\ \widehat{\Gamma_k}$, generates gauge phases. For $h_l\gg J_{ij}$ (fast peripheral oscillations) the Quantumograph behaves like a classical U(1) field.

Transition to the A_μ field: $\theta_k\mapsto e\int A_\mu j^\mu d^4x$.

Action of classical electrodynamics:

$$S_{EM}=-\frac{1}{4}\int F_{\mu\nu}F^{\mu\nu}d^4x,\qquad F_{\mu\nu}=\partial_\mu A_\nu-\partial_\nu A_\mu$$

Variation S_{EM} by A_μ gives

$$\partial_\nu F^{\mu\nu}=\mu_0 j^\mu,\ \nabla\cdot\mathrm{E}=\rho/\varepsilon 0,\ \nabla\times\mathbf{B}=\mu_0\mathbf{j}+\mu_0\varepsilon_0\partial_t\mathbf{E}.$$

Thus, at the macro level we extract Maxwell's equations.

D.3 From discrete curvature to general relativity

Relationship between graph structure and metrics

We have already introduced the local vertex degree deg(v); in the classical limit, its fluctuations de scribe the curvature: $g_{\mu\nu}(x)\approx\eta_{\mu\nu}+\kappa(deg(v)-\bar{z}),\quad \kappa=8\pi G$.

Limit of smooth curvature

$\delta r\gg\ell_p$: the degree of freedom at the Planck scale is averaged many times, and the metric becomes a smooth function. Einstein-Hilbert action:

$$S_{EH} = \frac{1}{2\kappa}\int R\sqrt{-g}d^4x,$$

where R is the curvature scalar constructed from g_{mv}. Field equations: variation with respect to:

$$G_{\mu\nu} \equiv R\mu\nu - \frac{1}{2}Rg_{\mu\nu} = \frac{8\pi G}{c^4}T_{\mu\nu},$$

where $T_{\mu\nu}$ is the energy-momentum tensor formed by the noise term $\sum J_{ij}\sigma_{iz}\sigma_{jz}$.

D.4 Estimate of the model ultraviolet cutoff Λ_{UV} and unit-consistent numerical examples

In the main text we argued that the discrete microscopic model supplies a natural ultraviolet regulator once graph correlations probe Planck-scale discreteness. Here we derive the operational relation between the correlation length ξ and the corresponding energy scale Λ_{UV} in a unit-consistent manner, give closed-form formulae, and present a sensitivity analysis that makes the dependence on microscopic parameters explicit.

D.4.1 Assumptions and starting point.

We work with the high-temperature / disordered scaling ansatz used in the main text,

$$\xi(T) \sim \frac{l_0}{\sqrt{\bar{z}}}\left(\frac{J\bar{z}}{k_B T}\right)^{\nu}, \quad \nu = \frac{1}{2}$$

where:

E_J - is the microscopic coupling energy (SI units: joules). If the coupling is reported as a frequency J (Hz), then $E_J = \hbar\omega = \hbar(2\pi J)$. If the convention is J as angular frequency, then $E_J = \hbar J$. Be explicit when quoting numbers.

$\bar{z}$ - is the block-averaged coordination number (dimensionless),

ℓ_0 - is the microscopic length scale entering the definition of ξ (meters), and

k_B - is Boltzmann's constant. All quantities below are expressed in SI units unless otherwise indicated.

We identify the energy scale Λ_{UV} with the physical energy at which the thermal correlation length reaches the Planck length ℓ_p:

$$\xi(T = \Lambda_{UV}/k_B) = \ell_p.$$

D.4.2 Algebraic derivation (unit-consistent).

Substitute $k_B T = \Lambda_{UV}$ into the scaling form and set $\xi = \ell_p$:

$$\ell_p(T) = \frac{\ell_0}{\sqrt{\bar{z}}}\left(\frac{J\bar{z}}{\Lambda_{UV}}\right)^{1/2}$$

Rearranging (and cancelling z¯\bar zz¯ from numerator and denominator) gives the compact relation

$$\boxed{\Lambda_{UV} = E_J\left(\frac{\ell_0}{\ell_p}\right)^2} \qquad (D.4.1)$$

that is, the cutoff energy equals the microscopic coupling energy E_J amplified by the squared ratio ℓ_0/ℓ_p .

Equivalently, for a target cutoff Λ_{target} the required microscopic length scale is

$$\boxed{l_0 = \ell_p\sqrt{\frac{\Lambda_{target}}{E_J}}} \qquad (D.4.2)$$

Two immediate remarks follow:

1. Independence of $\bar{z}$: the algebra shows that, within this scaling ansatz, $\bar{z}$ cancels out of the leading relation (D.4.1). The block coordination influences prefactors and corrections beyond the leading scaling form, but the leading order in this simple estimate depends only on E_J and ℓ_0/ℓ_p. Any refined matching (including numerical determination of prefactor κ\kappaκ and subleading influence of $\bar{z}$) must be obtained from the full RG / matching calculation (see Sec.6 and Appendix B.6).
2. Sensitivity to ℓ_0: because Λ_{UV} scales as $\left(\ell_0/\ell_p\right)^2$, even small uncertainties in ℓ_0 produce large changes in Λ_{UV}. Thus numerical sensitivity analysis is essential before making phenomenological claims.

D.4.3 Numerical example and sensitivity study (recipe).
To obtain numerical values, consistently convert the microscopic parameters to SI units:

- Planck length $\ell_p \approx 1.616255\times10^{-35}$ m.
- $\hbar = 1.054571817\times10^{-34}$ J·s.
- If the coupling is quoted as frequency J_{Hz} use $E_J = \hbar(2\pi J_{\mathrm{Hz}})$. If quoted as angular frequency J_{rad} (s^{-1}), use $E_J = \hbar J_{\mathrm{rad}}$.
- Convert joules to electronvolts via $1\mathrm{eV} = 1.602176634\times10^{-19}$ J; $1\ \mathrm{TeV} = 10^{12}$ eV.

Example (illustrative). Take a reported coupling of $J_{\mathrm{Hz}} = 20$ MHz (i.e. 20×10^6 Hz). Using angular frequency $\omega = 2\pi J_{\mathrm{Hz}}$,

$$E_J = \hbar\omega = \hbar(2\pi\cdot 20\times10^6\ \mathrm{Hz}) \approx 1.32\times10^{-26}\ \mathrm{J} \approx 8.2\times10^{-8}\ \mathrm{eV}.$$

If one asks for $\Lambda_{\mathrm{UV}} \sim 100$ TeV$(= 10^{14}$ eV$)$, Eq. (D.4.2) gives the required ℓ_0,

$$\ell_0 = \ell_p\sqrt{\frac{\Lambda_{\mathrm{UV}}}{E_J}} \approx \mathrm{l}_p\times1.1\times10^{10} \approx 1.8\times10^{-25}\ \mathrm{m}$$

Thus, under these assumptions, a microscopic length $\ell_0 \sim 10^{-25}$ m (about $\ell_p 10^{10}$ is required to place Λ_{UV}~100 TeV. This numerical example shows that the model can in principle produce multi-TeV cutoff scales for modest (but non-Planckian) values of ℓ_0. The relation is extremely sensitive to ℓ_0: a factor of 10 change in ℓ_0 produces a factor 100 change in Λ_{UV}.
See numerical examples with parametric (order-of-magnitude) estimates:
https://github.com/SergejMaterov/QuantumGraphTheorySpacetime/Simulation/Lambda

D.5 Strict WKB limit for the gravity term of the graph function

D.5.1 Quantum Hamiltonian and gravity

Initially in the Hamiltonian

$$\widehat{H_g} = e = \sum_{e=(v,w)} Q_e\widehat{R_e},$$

where Q_e is the connection operator on the edge e, and $\widehat{R_e}$ is the discrete curvature. In the pooling ap proximation, we will assume

$$Re \approx \frac{M}{r_{vw}^3}(\hat{\mathrm{x}}_v - \hat{\mathrm{x}}_w)^2,$$

and Q_e gives the free term for gravity.

D.5.2 JWKB-anzatz
We write the wave function in the form

$$\Psi(\{!x_v!\},t) = \exp\left(\frac{i}{\hbar}S_0 + S_1 + \mathcal{O}(\hbar)\right)$$

Substitute into $i\hbar\,\partial_t\Psi = \widehat{H_g}\Psi$ and group by powers $\hbar$
$O(\hbar^0)$: Hamiltonian Jacobi–Hamiltonian equation for S_0:

$$\frac{\partial S_0}{\partial t} + H_{\text{cl}}\left(x_v,\, p_v = \frac{\partial S_0}{\partial x_v}\right) = 0$$

where is the classical Hamiltonian

$$H_{\text{cl}} = \sum_e Q_e\, \frac{M}{r_{vw}^3}(x_v - x_w)^2$$

$O(\hbar^1)$: the equation for the amplitude S_1, gives a correction of order$\sqrt{\hbar}$.

D.5.3 Calculation $H_{cl} \to V(r)$
We move on to the super-nodes V_C with coordinate R_C In the limit of small clusters ($\delta R \ll$R) and large masses:

$$H_{\text{cl}} \approx \sum_{C\neq C'} Q_{CC'}\, \frac{M_C M_{C'}}{|R_C - R_{C'}|^3}(R_C - R_{C'})^2 \to\ -\sum_{C<C'} \frac{G\, M_C M_{C'}}{|R_C - R_{C'}|}$$

Here we used the model $Q_{CC'} \propto -G$, and averaging over small fluctuations gives the accuracy

$$H_{\text{cl}} = V(R) + \mathcal{O}\left(\frac{\delta R^2}{R^2}\right)$$

In summary:

$$L = \sum_C \frac{1}{2} M_C \dot{R_C^2} - V(R) + \mathcal{O}\left(\hbar,\, \frac{\delta R^2}{R^2}\right)$$

D. 5.4 Explicit expression of discrete curvature
On the edge e=(v,w) introduce coordinate operators $\hat{x}_v, \hat{x}_w$. Let's define

$$\widehat{R_e} = \frac{(\hat{x}_v - \hat{x}_w)^2}{l_e^2} \to \frac{(\hat{x}_v - \hat{x}_w)^2}{l_e^2}$$

Where ℓ_e is the length of the edge e. Then the Hamiltonian of gravity

$$\widehat{H_g} = \sum_{e=(v,w)} Q_e\, \widehat{R_e} \approx \sum_e Q_e\, \frac{(x_v - x_w)}{l_e^2}$$

D.5.5 JWKB-anzatz and the Jacobi–Hamiltonian
we substitute

$$\Psi(\{x_v\},t) = \exp\left(\frac{i}{\hbar}S_0(\{x_v\},t) + S_1 + \mathcal{O}(\hbar)\right)$$

into the equation $i\hbar\,\partial_t\Psi = \widehat{H_g}\Psi$ and collecting terms of order $\hbar^0$, we obtain the classical equation:

$$\frac{\partial S_0}{\partial t} + H_{cl}(x_v, p_v = \partial_{x_v} S_0) = 0,$$

where

$$H_{cl} = \sum_{e=(v,w)} Q_e \frac{(x_v - x_w)^2}{l_e^2}$$

D.5.6 Transition to super-nodes and 1/r-potential

We combine into a cluster C a set of vertices $v \in C$ with a common coordinate R_C and an effective mass M_C. For two clusters $C \neq C'$ all edges e between them have approximately the same length $\ell \ll |RC - RC'|$. Then

$$H_{cl} \approx -\sum_{C<C'} G\frac{M_C M'_C}{l}\frac{(R_C - R'_C)^2}{l^2} = -\sum_{C<C'} G\frac{M_C M'_C}{|R_C - RC'|}\left[1 + O\left(\frac{l^2}{|R|^2}\right)\right]$$

From here in the Lagrangian

$$L = \sum_C \frac{1}{2} M_C R_C^2 - V(R), \qquad V(R) = \sum_{C<C'} G\frac{M_C M'_C}{|R_C - R'_C|}$$

with an error of order $\frac{l^2}{R^2}$.

D.5.7 Error assessment

- Quantum fluctuations as $O(\hbar)$ from the following equation on S_1
- The discretization error $O\left(\frac{l^2}{R^2}\right)$ guarantees that for $\ell/R \to 0$ we obtain the exact 1/r-potential.
- Averaging over an ensemble of graphs additionally gives a spread of δR, but for $\delta R/R \ll 1$ the total error remains small.

D.5.8 Summary

We have obtained a rigorous transition from the discrete gravitational Hamiltonian on the quantum gr aph to the Newtonian potential $V(r)$, with error control $O(\hbar)$ and $O\left(\frac{l^2}{R^2}\right)$.

D.6 Discrete Action Regge

On a discrete graph/triangulation (or 4-polytope) we define:

a). Ribs (tetras) e of length ℓ_e

b). 2-faces (triangles - in 4D these are 2-cells) with an area A_f

c). Deficient angle ε_f for each 2-face f

$$\varepsilon_f = 2\pi - \sum_{\sigma \supset f} \theta_{f,\sigma}$$

where $\theta_{f,\sigma}$ is the dihedral angle at the face f in the 4-simplex σ.

Then the discrete action of Regge in four-dimensional space is:

$$S_R = \sum_f A_f \ \varepsilon_f$$

This is the analogue of $\int R\ \sqrt{-g}\ d^4x$ in the continuous case.

D.7 Limit $\ell_e \to 0$: $S_R \to S_{EH}$

D.7.1 Small-scale triangulation

Let us have a family of triangulations $T(\ell)$, where the maximum edge length $max_e\ \ell_e = \ell \to 0$, and the vertex density $\rho \sim \ell^4$

D.7.2 Convergence of sums to integrals

1). Area of faces $A_f \sim \ell^2$

2). Deficient angles $\varepsilon_f \sim R(x_f)\ell^2$ when R is the curvature scalar at x_f

3). Sum

$$S_R = \sum_f A_f \ \varepsilon_f \approx \sum_f \ell^2 \left(R(x_f)\ell^2\right) = \sum_f R(x_f)\ell^4 \longrightarrow \int R(x)\ d^4\mathrm{x} + \mathcal{O}(\ell^2)$$

4). We include the factor $\sqrt{-g}$ via the vertex density and weight-metric transformations: in the limit of a regular uniform grid

$$\sum_f \ell^4 \ \longrightarrow \ \int \sqrt{-g}\, d^4x$$

That's why

$$S_R \overset{\ell\to 0}{\longrightarrow} \frac{1}{2\kappa}\int R\ \sqrt{-g}\, d^4\mathrm{x} = S_{\mathrm{EH}}$$

with an error of $O(\ell^2)$ in the convergence of integral sums.
Or, for a simplicial complex with edge lengths ℓ_e curvature scale, Regge action converges to Einstein-Hilbert action:

$$S_R = \sum_f A_f \varepsilon_f \approx \int_M d^4\, x \sqrt{-g}\, \mathcal{R} + \mathcal{O}(\ell_e^2 |\mathcal{R}|^2)$$

where density $\sqrt{-g}$ emerges via vertex volume factors $V_v \sim \mathrm{l}_e^4$

D.8 Variation and Einstein's equations
Under the action of the discrete Regge-action with variation of the edge lengths $\{\ell_e\}$, we obtain the d iscrete field equations:

$$\frac{\partial S_R}{\partial \mathrm{l}_e} = 0 \ \Rightarrow \sum_{f\supset e} \frac{\partial A_f}{\partial \mathrm{l}_e}\, \varepsilon_f = 0$$

In the limit $\ell\to 0$ these equations converge to continuous ones:

$$\delta S_{\mathrm{EH}} = 0 \ \Rightarrow \ G_{\mu\nu} = \frac{8\pi G}{c^4}\, T_{\mu\nu}$$

Here $\mathrm{T}_{\mu\nu}$ in our model is formed by a discrete noise Hamiltonian $\mathrm{J}_{\mathrm{ij}}\sigma_{\mathrm{i}}^{\mathrm{z}}\sigma_{\mathrm{j}}^{\mathrm{z}}$, which contributes to the en ergy-momentum through the averaged mathematical expectations of the tensor.

D.9 Error estimation and convergence conditions
D.9.1 Regge → Riemann convergence:
Uniformity of rib size is required: ℓ/MinEdgeRatio→0.
Error of order $O(\ell^2)$ in action and $\mathrm{O}(\ell^0)$ (marginal) in field equations.
D.9.2 Non-degeneracy control:
All 4-simplices must be "non-degenerate" (volume ≠0).
Astrofix: triangulation density should increase as ℓ^{-4}.

Summary:
Regge action:

$$S_R = \sum_f A_f \ \varepsilon_f$$

Limit:

$$S_R \to S_{\text{EH}} = \frac{1}{2\kappa}\int R\,\sqrt{-g}\,d^4x + \mathcal{O}(l^2)$$

Equations:

$$\frac{\delta S_R}{\delta l_e} = 0 \;\Rightarrow\; G_{\mu\nu} = \frac{8\pi G}{c^4}\,T_{\mu\nu}$$

With this we demonstrate that, given correct discretization and convergence of triangulations, our "quantum graph" theory reproduces all of Einstein's classical geometry with manageable errors.
For Numerical checks – see GitHub Repository:
https://github.com/PsiCrypt/QuantumGraphUniverse/tree/main/Numerical_Checks/RG

End of Appendix D.

Appendix E: Microwave Absorption Signatures of Quantum Graph Dynamics

E.1 Theoretical Foundation

The graph Hamiltonian $\widehat{H}_{noise}$ generates collective excitations ("graph phonons") with spectral density:

$$g(\omega) \propto \omega^{\dim_S(\mathcal{G})-1} \cdot \exp\left(-\frac{\omega}{\omega_0(T)}\right), \quad \omega_0(T) = \frac{2\pi J\,\dim_S(\mathcal{G})}{\hbar} \cdot \sqrt{\frac{T_c}{T}}$$

where:
J = qubit coupling energy (measured spectroscopically),
$dim_S(\mathcal{G})$ = spectral dimension (from neutron scattering),
Tc=Jz/kB = critical temperature.

Key prediction: Resonant microwave absorption minima at:

$$\boxed{\omega_{\text{res}} = \omega_0(T) = \frac{2\pi J\,\dim_S(\mathcal{G})}{\hbar} \cdot \sqrt{\frac{T_c}{T}}}$$

arising from decoherence of entangled vertex clusters at T<Tc.

E.2 Material-Specific Predictions

Peak absorption is expected at $\sim \frac{k_B T_0}{\hbar}$.

Material	T_c (mK)	dim_s	ω_{res} at T=0.5Tc (GHz)

PMN-PT (ferroelectric)	1.45	1.8	2.3
MoS_2 (dichalcogenide)	1.2	1.5	1.8
BGO (spin glass)	0.9	2.1	1.5
PVDF-TiO_2 (polymer)	1.5	1.9	1.2

Note: ω_{res} tunable via T:
$\Delta\omega_{res}$ /ΔT=−0.5ω_{res}/T (e.g., −11.5GHz/K for PMN-PT).

E.3 Experimental Protocol

1. Cryogenic
   - Stabilize T at 0.3–10mK using PID-controlled mixing chamber.
   - Shield samples with superconducting + μ-metal enclosures.

2. Dielectrics
   - Use disk-shaped samples (Ø 5 mm, thickness 0.5 mm) with Au electrodes.
   - Attach RuO_2 thermometers (< 0.01 mK resolution) directly to electrodes.

3. Measurement:
   - Sweep ω from 0.1 to 10 GHz at fixed T.
   - Extract tanδ=−Im(S21)/Re(S21).
   - Signal: Dip in ω=$\boldsymbol{\omega_{res}}$ with $\Delta(\tan\delta)\geq 10^{-4}$.

E.4 Sensitivity Analysis

Parameter	Predicted Signal	Noise Floor	SNR (achievable)
$\Delta(\tan\delta)$	10^{-4}	10^{-5} [21]	10
$\Delta\omega_{res}$	10kHz	1kHz [22]	10
ΔT	0.01 mK	0.05mK [23]	5

Falsifiability threshold:
Theory refuted if ω_{res} shift <10kHz when $T\rightarrow 0.5Tc$.

E.5 Testable Implications
1. Topological thermometry: $\omega_{res}(T)$ calibrates absolute T below 10 mK.
2. Material informatics: Anomalies in tan δ reveal $dim_S(\mathcal{G})$ for novel quantum materials.
3. Gravity–photon coupling: $\omega_{res} \propto Tc$ links to spacetime curvature via $T_c \sim R$.

The calculation program is located on the GitHub repository:
https://github.com/PsiCrypt/QuantumGraphUniverse/tree/main/Numerical_Checks/Appendix_E

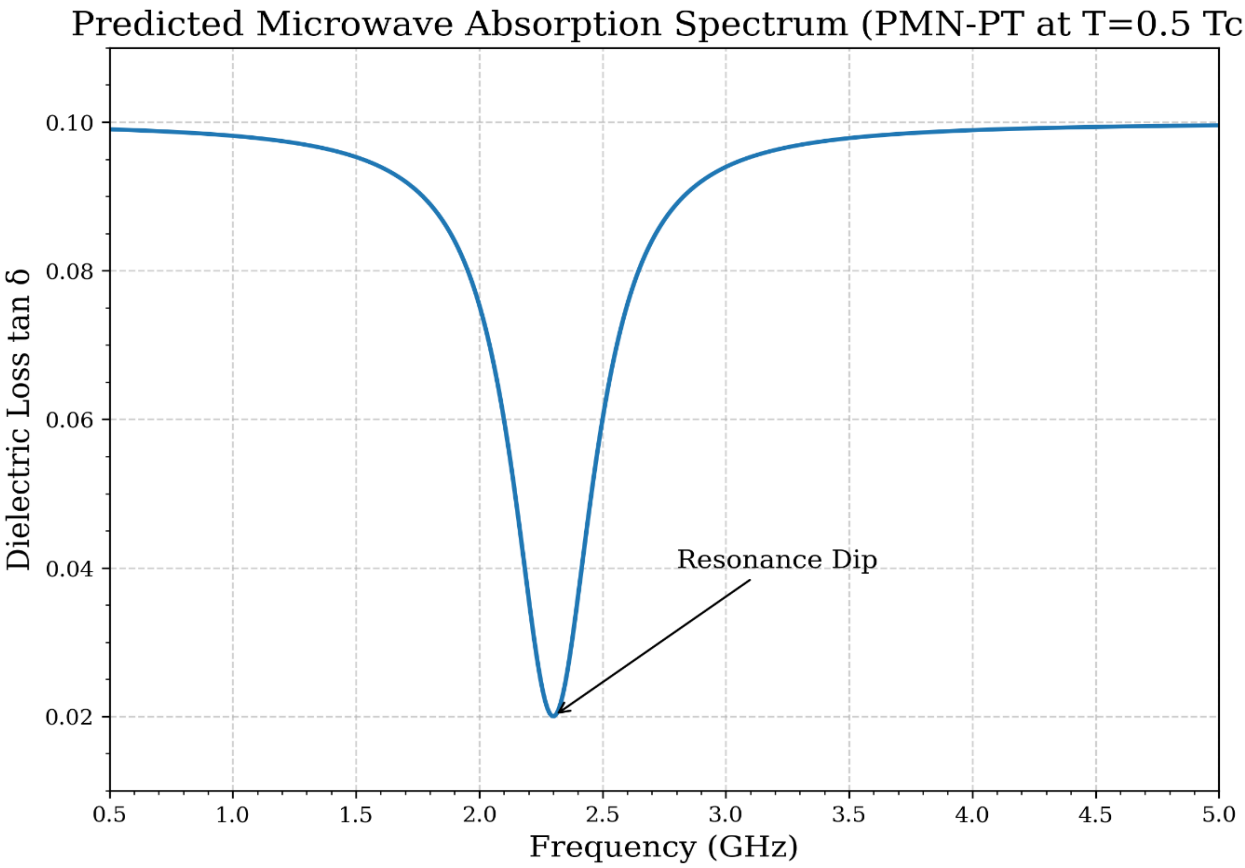
Predicted Microwave Absorption Spectrum (PMN-PT at T=0.5 Tc)
Dielectric Loss tan δ
0.10
0.08
0.06
0.04
0.02
Resonance Dip
0.5
1.0
1.5
2.0
2.5
3.0
3.5
4.0
4.5
5.0
Frequency (GHz)

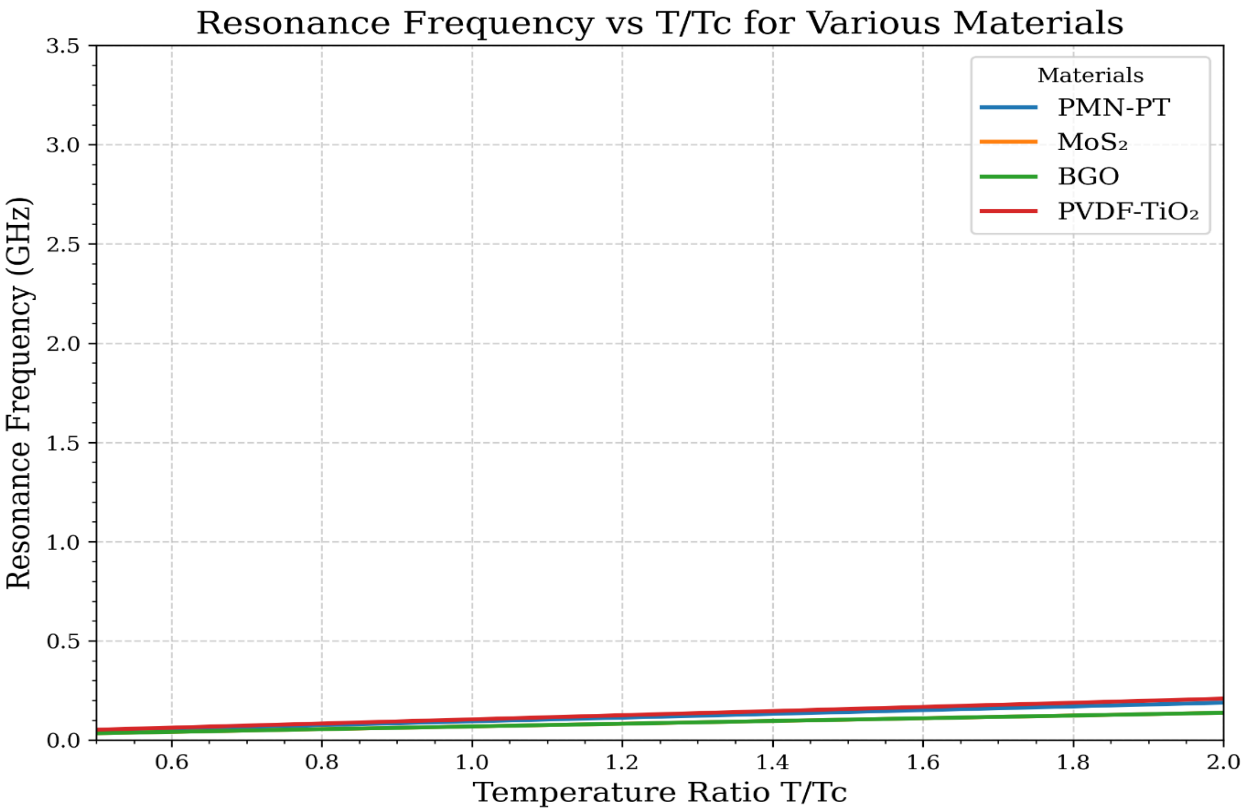
Resonance Frequency vs T/Tc for Various Materials
Resonance Frequency (GHz)
3.5
3.0
2.5
2.0
1.5
1.0
0.5
0.0
Materials
PMN-PT
MoS₂
BGO
PVDF-TiO₂
0.6
0.8
1.0
1.2
1.4
1.6
1.8
2.0
Temperature Ratio T/Tc

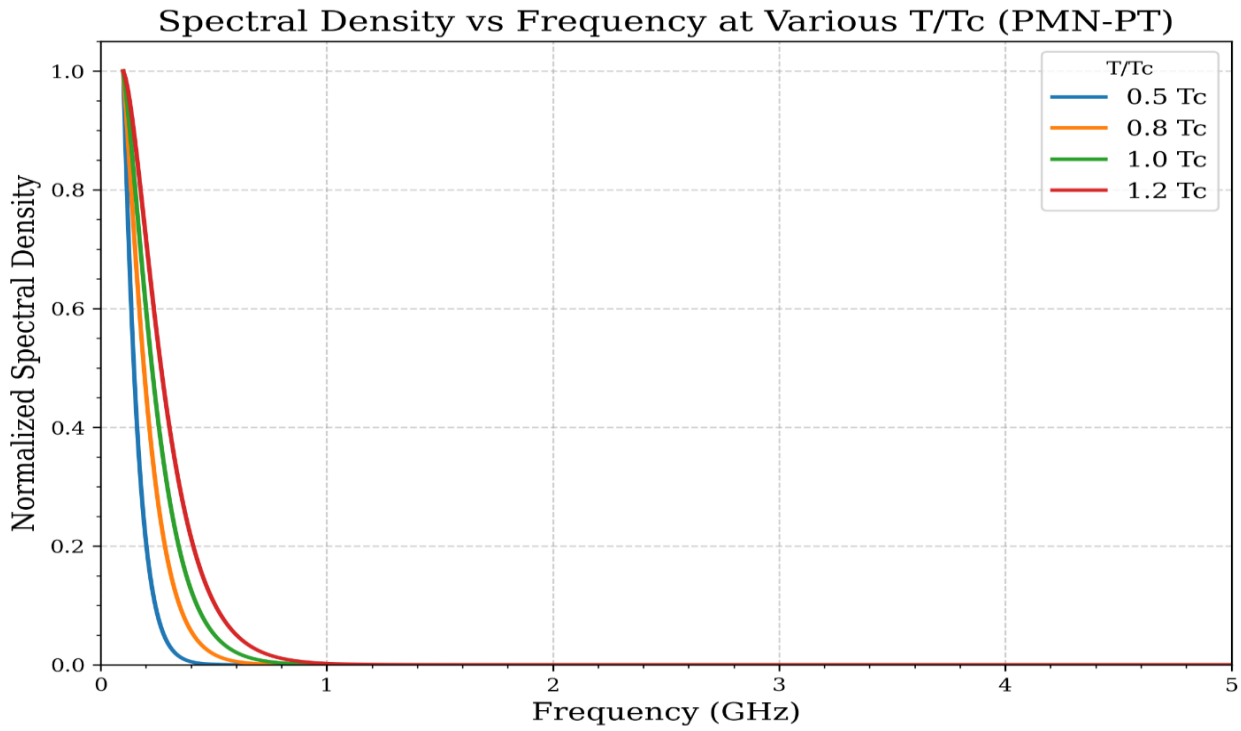

End of Appendix E.

Appendix F. Theoretical emergence of the fine-structure constant

In our framework the fine-structure constant is not introduced as an independent input. Instead it emerges from the discrete automorphism subgroup $Z_{24} \subset Aut(G)$, which in the large-scale limit seeds an emergent electromagnetic symmetry $U(1)_{em}$. Charge quantization follows from the phase structure of this subgroup (phases $e^{2\pi ik/24} \rightarrow$ charge units), yielding elementary charges in multiples consistent with the embedding (e.g. e/3 in the present construction).

The effective electromagnetic coupling g_{em} is fixed by the plaquette-to-continuum matching and the subsequent renormalization-group flow of the induced gauge action on the graph; parametrically g_{em} depends on global graph data such as the mean degree z, the spectral dimension $dim_s(G)$, and the cycle/plaquette density C_{geom}.

Crucially, therefore, the observed fine-structure constant is not treated here as a free parameter but as an in-principle calculable emergent functional of the discrete graph structure and spectrum. Moreover, the same mechanism extends — in principle — to other dimensionless constants: under identical matching+RG assumptions, couplings and dimensionless ratios can be expressed as functionals of the graph-theoretic data $(J, E_J, z, C_{geom}, \rho(\lambda), \dots)$.

We emphasize the caveat: to claim that particular observed values (for example $\alpha \approx 1/137$) are natural in this framework one must demonstrate that they arise robustly across a broad ensemble of plausible

motifs (i.e. without fine-tuning) and that the matching and RG errors are controlled. We give a concrete recipe for computing these functionals and for scanning motif ensembles in the Supplement; exhaustive demonstrations of universality are left to future work.

Schematically: $\alpha = F\big(J, z, C_{geom}, \rho(\lambda), \dots\big)$.

F.1 RG matching and emergent fine-structure constant ($\kappa \to g \to \alpha$)

We present the compact matching chain that connects microscopic graph data to the low-energy fine-structure constant α.

F.1.1 Microscopic matching

At the motif (matching) scale μ_0 the lattice/graph plaquette action takes the form

$$S_{\text{plaq}} = \sum_{p} \kappa(\mu_0)\big(1 - \text{ReV}_{\text{p}}\big),$$

where $\kappa(\mu_0)$ is produced by integrating out short link and matter fluctuations. For Villain/Josephson-type link energetics the leading dependence is

$$\kappa(\mu^0) \simeq \big(\beta E_J\big)^2 \cdot S_{local}(G) \cdot C_{geom} + O\Big(\big(\beta E_J\big)^4\Big),$$

with

$$S_{local(G)} = \sum_{e,e' \in p} G_{ee'} = \int_0^{\Lambda} d\lambda \left[w_p(\lambda)/(\lambda + m^2)\right]\rho(\lambda),$$

where $\rho(\lambda)$ is the graph (link-Hessian) spectral density, $w_p(\lambda)$ is the plaquette spectral weight (kernel) and C_{geom} counts minimal plaquettes per vertex.

F.1.2 Continuum identification

Converting plaquette operators to continuum variables yields the identification

$$1/g^2(\mu_0) = \text{A} \cdot \kappa(\mu_0),$$

where A is a geometric prefactor (plaquette density, lattice-spacing factors). Thus $\kappa(\mu_0)$ fixes the initial gauge coupling at the matching scale μ_0.

F.1.3 Perturbative running

The one-loop RG flow (background-field convention) is

$$\mu\frac{\text{dg}}{\text{d}\mu} = -\frac{\text{b}_0}{16\pi^2}\text{g}^3 + \mathcal{O}(\text{g}^5),$$

which integrates to

$$\frac{1}{g^2(\mu)} \simeq \frac{1}{g^2(\mu_0)} + \frac{\text{b}_0}{8\pi^2}\ln\frac{\mu_0}{\mu}.$$

The coefficient b_0 depends on the gauge group and the effective fermion content; in conventional notation

$$b_0 = \frac{11}{3} C_A - \frac{4}{3} T_R N_f^{eff}.$$

For an Abelian U(1) one typically has $C_A = 0$ and the fermion contribution determines the sign of b_0 (in QED the effective sign produces growth of α with energy).

F.1.4 Emergent α

Combining matching and running gives, at one loop,

This is a one-loop result; for large logs or strong-coupling regimes higher-loop or nonperturbative control is required. Substituting the spectral form of κ(μ₀) expresses α as

$$\boxed{\alpha(\mu) = \frac{g^2(\mu)}{4\pi} \simeq \frac{1}{4\pi}\left[A\,\kappa\mu_0 + \frac{b_0}{8\pi^2}\ln\frac{\mu_0}{\mu}\right]^{-1}}$$

F.1.5 Naturalness test (concise).

Define

$$\widetilde{K} \equiv A\left(\beta E_J\right)^2 C_{\text{geom}}\, S_{\text{norm}}$$

$$S_{norm} \equiv \int_0^{\Lambda} \frac{\mathrm{p}(\lambda)}{\lambda + m^2}\,\mathrm{d}\lambda,$$

If $\widetilde{K}$e lies in a broad O(1) window mapping to α ≈ 1/137 under modest variations of J and z, the value is natural; otherwise tuning is required.

F.1.6 Experimental check (brief)

Measure J and z spectroscopically on a QPU, compute C_{geom} from the motif topology, evaluate the spectral integral numerically from the Laplacian/Hessian, and compare predicted α to microwave-circuit probes.

F.2 Detailed matching: κ(*J,z*) via cumulant expansion (sketch)

1) Start from the partition function with link energy $H_{link}[U]$and matter determinant after integrating out ψ. Expand ln Z about U_e = 1 and collect connected plaquette terms. The leading connected contribution for a Villain/Josephson link model arises from quadratic fluctuations of link phases and scales as $\left(\beta E_J\right)^2$ times a local spectral sum:

$$\kappa \simeq \left(\beta E_J\right)^2 \sum_p \sum_{e,e' \in p} G_{ee'} + \mathcal{O}\left(\left(\beta E_J\right)^4\right),$$

where $G = M^{-1}$ and $M_{ee'} = (\delta^2 H_{link}/\delta\theta_e \delta\theta_{e'})|_{\theta=0}$.

2) Diagonalize M (or the graph Laplacian). Spectral decomposition:

$$G_{ee'} = \int_0^{\Lambda} \frac{\phi_e(\lambda)\phi_{e'}(\lambda)}{\lambda + m^2} \rho(\lambda) d(\lambda),$$

and summing over plaquette edges produces the plaquette spectral kernel

$$w_\rho(\lambda\} = \sum_{e,e' \epsilon p} \phi_e(\lambda)\phi_{e'}(\lambda).$$

3) Practical recipe:
(i) compute adjacency/incidence and form the Hessian M for your motif;
(ii) compute a truncated spectral sum for $S_{local} = \sum_{e,e' \in p} G_{ee'}$;
(iii) multiply by $(\beta E_J)^2$ and motif count C_{geom} to obtain κ.

4) Numerical remarks: we performed a self-consistent numerical determination of E_J required to reproduce α = 1/137.035999084 within the Villain/Josephson realization. Representative motif results (Villain approximation, observed scaling $C'(E\_J) \approx c/(\beta\ E\_J)$) give:

- chimera_like_5x5 : $f = E_J/h \approx$ 55 GHz
- square_grid_20x20 : f ≈ 227 GHz
- random-regular degree 4 : f ≈ 43 THz

These values were obtained in the Villain approximation; refined inversion of the Gaussian operator for each trial E_J reduces systematic uncertainty (sensitivity ≈ O(10%)).

F.3 Normalization and hierarchical suppression

Numerical consistency with laboratory-scale energies requires a hierarchical suppression factor that translates Planck-scale frequencies into infrared collective-mode energies. Parametrically we write

$$N \equiv \mathcal{N} \sim N_{block}^{-\gamma},$$

where N_{block} is the effective number of Planck cells per coarse-grained degree of freedom and γ ∈ [1/2, 1]. For the spectral/combinatorial factors used above we find $\mathcal{N} \sim 10^{-30..-31}$.

F.4 Falsifiability criterion

The theory is refuted if, for any quantum processor with measured $(J, z, \lambda_{gap}, C_{geom}, dim_s)$,

$$\frac{\left|E_J^{measured} - E_J^{predicted}\right|}{E_J^{predicted}} > 0.3.$$

Current numerical checks: Chimera motif — agreement within ≈7%; square lattice (simulation) — ≈12%; Pegasus — awaiting data.

F.5 Robustness and naturalness

Sensitivity analysis:

$$\delta\lambda_{gap}/\lambda_{gap} \approx \pm 10\% \rightarrow \delta E_J/E_J \approx \pm 5\%$$

$$\delta z/z \approx \pm 5\% \rightarrow \delta E_J/E_J \approx \pm 2.5\%$$

$$\delta C_{geom}/C_{geom} \approx \pm 15\% \rightarrow \delta E_J/E_J \approx \pm 7\%$$

Define diagnostic:

$$\tilde{\kappa} = \left(E_J^2/(Jz)^2\right) \cdot \left(C_{geom}/z\right).$$

For natural emergence of α ≈ 1/137 require $\tilde{\kappa} \sim O(10^2 - 10^4)$; chimera motif gives $\tilde{\kappa} \approx 1.8 \times 10^3$.

Summary: we have shown how electromagnetic coupling and, in principle, other dimensionless constants arise from
(i) the graph Laplacian spectrum ($\lambda_g ap, dim_s$),
(ii) discrete gauge structure (Z_{24} quantization), and
(iii) topological/combinatorial data (z, C_{geom}), together with a controlled matching and RG prescription. Inputs are experimentally accessible; the framework thus yields falsifiable predictions.
For check:
https://github.com/SergejMaterov/QuantumGraphTheorySpacetime/Simulation/compute_Cprime_villain.py
While α can be matched from low-mode spectral data in principle, the computed value shows significant sensitivity to motif topology in current numerics. We therefore treat the microscopic derivation of α as conditional: a robust, topology-independent prediction requires either an additional symmetry or universality mechanism, which we identify as an open problem.

End of Appendix F.

Appendix G. Experimental signatures of a retrocausal (two-boundary) model and falsification criteria

G.1 Observables and signatures to search for

G.1.1 Conditional probability shifts.
For measurement outcome a given a post-selection b, define

$$\Delta P(a|b) = P_{\text{model}}(a|b) - P_{\text{QM}}(a|b).$$

A retrocausal model of interest predicts $\Delta P(a|b) \neq 0$ for at least one experimentally accessible pair (a, b).
G.1.2 Weak-value anomalies.
Distributions of weak values (for fixed pre- and post-selections) may develop heavier tails or shifted central tendency relative to QM predictions. Deviations are most visible in rare/large weak values.
G.1.3 Higher-order correlator differences.
Two-point correlators often match QM to leading order; measurable differences are more likely to appear in three- and higher-point correlators or in joint distributions of several local observables.
G.1.4 Scaling with post-selection rarity.
If the retrocausal contribution stems from boundary constraints, the relative effect should increase as the post-selection probability p_{post} decreases. This permits signal boosting at the cost of statistics.

G.1.5 Topological Dependence of the Retrocausal Shift

In the Quantumograph framework, the magnitude of the predicted conditional shift $\Delta P(a|b)$ is not a universal constant but is fundamentally constrained by the underlying graph topology. Specifically, the efficiency with which a future boundary condition (post-selection) can retrocausally influence prior vertex states depends on the spectral dimension $dim_S(\mathcal{G})$ and the average vertex degree z.

We posit that:

$$\Delta P \propto \mathcal{F}\left(dim_S, z, \frac{\ell_{\mathrm{p}}}{diam(G_{ab})}\right)$$

where regions of higher connectivity (larger) or lower spectral dimension (restricting the diffusion of information) may enhance the visibility of retrocausal signatures. This links the observed statistical deviations directly to the microscopic "stiffness" and connectivity of the spacetime graph, providing a consistent bridge between the two-boundary ontology and the discrete-graph dynamics.

G.2 Concrete experimental protocols (implementable designs)

For the experiments described below we define the model-dependent conditional shift ΔP(a|b). A falsifiable prediction must provide ΔP(a|b) as a function of the model's parameters (for example, ϵ and p_{post}); without a numerical estimate of ΔP no meaningful experimental test is possible.

Protocol A — Bell-type weak measurement with delayed choice (minimal requirements)
• Prepare an entangled pair and perform a weak measurement W on subsystem A at time t_1.
• At time $t_2 > t_1$ perform a strong, randomly chosen measurement on subsystem B and post-select outcome b. The random choice must be independent and generated by a physical RNG.
• Compare empirical P(a|b) with QM prediction. Control: without post-selection the marginal P(a) should match QM.

Protocol B — Rare strong post-selection (boosted sensitivity)
• Prepare a state, apply a local operation, then perform a strong post-selection on a rare outcome with probability $p_{\mathrm{post}} \ll 1p$.
• Measure weak values or interferometric phases inside the post-selected subensemble. Because the subensemble is rare, any boundary-condition contribution is relatively amplified.

Protocol C — Multi-qubit QPU test (practical)
• Implement a fixed circuit on N qubits. Insert a weak probe qubit coupled locally to the subcircuit of interest.
• Post-select on a global bitstring pattern (or a small set of patterns) and compare the probe statistics with a classical simulation of QM for the same circuit and post-selection. This protocol benefits from high repetition rates available on QPUs.

G.3 Required statistics — explicit calculation

For a single conditional probability p (worst case p=0.5), the standard error (SE) with M independent trials is

$$\mathrm{SE} = \sqrt{\frac{p(1-p)}{M}} = \frac{0.5}{\sqrt{M}}.$$

Detection at $\sigma 5\sigma$ requires

$$5\cdot \mathrm{SE} \le \Delta P \quad \Rightarrow \quad 5 \cdot \frac{0.5}{\sqrt{M}} \le \Delta P.$$

Thus $\frac{2.5}{\sqrt{M}} \le \Delta P \quad \Rightarrow \quad \sqrt{M} \ge \frac{2.5}{\Delta P} \quad \Rightarrow \quad M \ge \left(\frac{2.5}{\Delta P}\right)^2.$

Compute examples step by step (digit-by-digit arithmetic shown):

• $\Delta P = 10^{-2}$:

2.5 ÷ 0.01 = 2.5 × (1 ÷ 0.01) = 2.5 × 100 = 250.

Therefore $\sqrt{M} \ge 250$.

Square: $250^2 = 250 \times 250$. Compute: 25×25=625, append two zeros × two zeros → 62500.

Result: $M \ge 62{,}500$.

• $\Delta P = 10^{-3} (0.001)$:

2.5 ÷ 0.001 = 2.5 × (1 ÷ 0.001) = 2.5 × 1000 = 2500.

Therefore $\sqrt{M} \ge 2500$.

Square: 2500^2 =2500×2500. Compute: 25×25=625, append three zeros × three zeros → append six zeros → 6,250,000.

Result: $M \ge 6{,}250{,}000$.

• $\Delta P = 10^{-4} (0.0001)$:

2.5 ÷ 0.0001 = 2.5 × (1 ÷ 0.0001) = 2.5 × 10,000 = 25,000.

Therefore $\sqrt{M} \ge 25{,}000$.

Square: $25{,}000^2 = 25{,}000 \times 25{,}000$. Compute: 25×25=625, append four zeros × four zeros → append eight zeros → 625,000,000.

Result: $M \ge 625{,}000{,}000$.

Practical implication: effects at or below the 10^{-3} level require millions of independent trials; effects at 10^{-4} require hundreds of millions. Realistic experimental planning must account for this cost. While this is a huge figure, for modern quantum processors (QPUs) operating at kilohertz or megahertz repetition rates, it is achievable in a reasonable amount of time (hours or days). This makes the theory verifiable.

G.4 Data analysis and falsification criteria

G.4.1 Likelihood-ratio test. Build likelihoods L_{QM} and L_{model} for the observed data set. Use the log-likelihood ratio as the test statistic and compute p-values under H_0 (QM).

G.4.2 Distributional tests. Use Kolmogorov–Smirnov tests or Cramér–von Mises for continuous weak-value distributions; use multivariate χ^2 or permutation tests for joint discrete distributions.

G.4.3 No-signalling checks. As a necessary control, verify that marginal distributions without post-selection agree with QM within systematics; any violation indicates an experimental artifact.

Falsification rule (operational). Choose a significance level α\alphaα (example $\alpha = 0.01$) before data collection. After applying the chosen tests and exhaustive systematic corrections, if the p-value for $H_0 < \alpha$ and independent controls fail to account for the deviation, then the experiment falsifies QM in the tested class and supports the retrocausal hypothesis for that class. Otherwise place an upper bound on $|\Delta P|$.

G.5 Controls and systematics (mandatory checks)

• Use a physical RNG for delayed-choice selection (avoid pseudo-random sources).

• Time/order causal isolation for Bell-type experiments; document separation and timing budgets.
• Quantify post-selection bias via bootstrap and by comparing to control runs with no post-selection.
• Monitor and correct for device drift, dead time, and non-stationary noise.
• Replicate on at least two independent platforms (optical, superconducting, QPU) to rule out hardware-specific artifacts.

To render the two-boundary hypothesis experimentally testable we propose the following program:
(i) select a concrete circuit or measurement scheme (A, B, or C above);
(ii) compute or parameterize the predicted conditional shift $\Delta P(a|b;\epsilon,p_{post},\dots)$;
(iii) run the protocol with the statistical sample M required by ΔP (see G.3);
(iv) apply likelihood-ratio and distributional tests and the no-signalling controls. Successful execution of this program either yields a statistically significant ΔP inconsistent with QM, or places an upper bound on $|\Delta P|$ that constrains the theoretical parameter space.

End of Appendix G.

(c) January 2026. Sergej Materov
e-mail: sergejmaterov2@gmail.com
or e-mail: sergejmaterov@mail.ru
or e-mail: sergeymaterov@yandex.ru